Cell protrusions and contractions generate long-range membrane tension propagation

Henry de Belly, Shannon Yan, Hudson Borja da Rocha, Sacha Ichbiah, Jason P Town, Patrick J Zager, Dorothy C Estrada, Kirstin Meyer, Hervé Turlier, Carlos Bustamante, et al.

Cell

Cell protrusions and contractions generate long-range membrane tension propagation

Graphical abstract

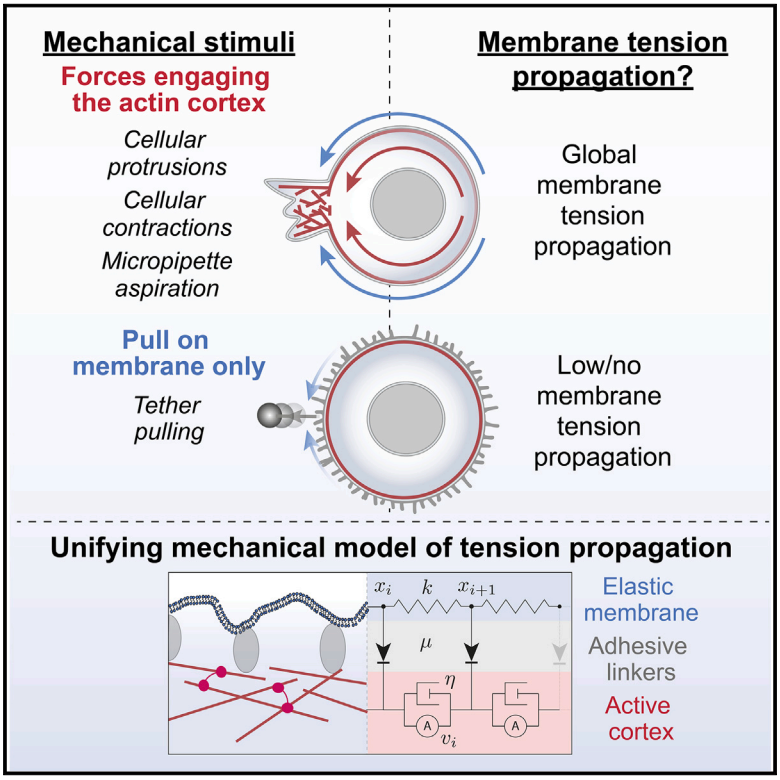

Highlights

- Forces engaging actin cortex generate rapid long-range membrane tension propagation
- Forces applied to cell membrane alone fail to propagate membrane tension
- Unifying mechanical model explains the requirements for membrane tension propagation
- Membrane tension is consistent with a long-range integrator of cell physiology

Authors

Henry De Belly, Shannon Yan, Hudson Borja da Rocha, ..., Hervé Turlier, Carlos Bustamante, Orion D. Weiner

Correspondence

herve.turlier@college-de-france.fr (H.T.), carlosjbustamante2@gmail.com (C.B.), orion.weiner@ucsf.edu (O.D.W.)

In brief

Experiments and modeling reveal the requirements for rapid and robust membrane tension propagation.

De Belly et al., 2023, Cell *186*, 3049–3061
July 6, 2023
https://doi.org/10.1016/j.cell.2023.05.014

CellPress

Cell

CellPress
OPEN ACCESS

Article

Cell protrusions and contractions generate long-range membrane tension propagation

Henry De Belly,[1,2,10] Shannon Yan,[3,4,10] Hudson Borja da Rocha,[5] Sacha Ichbiah,[5] Jason P. Town,[1,2] Patrick J. Zager,[1,2] Dorothy C. Estrada,[1,2] Kirstin Meyer,[1,2] Hervé Turlier,[5,*] Carlos Bustamante,[3,4,6,7,8,9,*] and Orion D. Weiner[1,2,11,*]

[1]Cardiovascular Research Institute, University of California, San Francisco, San Francisco, CA, USA
[2]Department of Biochemistry and Biophysics, University of California, San Francisco, San Francisco, CA, USA
[3]Department of Molecular and Cell Biology, University of California, Berkeley, Berkeley, CA 94720, USA
[4]California Institute for Quantitative Biosciences, University of California, Berkeley, Berkeley, CA 94720, USA
[5]Center for Interdisciplinary Research in Biology (CIRB), Collège de France, CNRS, Inserm, Université PSL, Paris, France
[6]Jason L. Choy Laboratory of Single-Molecule Biophysics, University of California, Berkeley, Berkeley, CA, USA
[7]Department of Physics, University of California, Berkeley, Berkeley, CA, USA
[8]Howard Hughes Medical Institute, University of California, Berkeley, Berkeley, CA, USA
[9]Kavli Energy Nanoscience Institute, University of California, Berkeley, Berkeley, CA, USA
[10]These authors contributed equally
[11]Lead contact
*Correspondence: herve.turlier@college-de-france.fr (H.T.), carlosjbustamante2@gmail.com (C.B.), orion.weiner@ucsf.edu (O.D.W.)
https://doi.org/10.1016/j.cell.2023.05.014

SUMMARY

Membrane tension is thought to be a long-range integrator of cell physiology. Membrane tension has been proposed to enable cell polarity during migration through front-back coordination and long-range protrusion competition. These roles necessitate effective tension transmission across the cell. However, conflicting observations have left the field divided as to whether cell membranes support or resist tension propagation. This discrepancy likely originates from the use of exogenous forces that may not accurately mimic endogenous forces. We overcome this complication by leveraging optogenetics to directly control localized actin-based protrusions or actomyosin contractions while simultaneously monitoring the propagation of membrane tension using dual-trap optical tweezers. Surprisingly, actin-driven protrusions and actomyosin contractions both elicit rapid global membrane tension propagation, whereas forces applied to cell membranes alone do not. We present a simple unifying mechanical model in which mechanical forces that engage the actin cortex drive rapid, robust membrane tension propagation through long-range membrane flows.

INTRODUCTION

For proper physiology, cells need a way to link short-range biochemical signaling events to long-range integration of cell-wide behaviors. Membrane tension is thought to serve as this global coordinator during cell migration. Membrane tension is the resistance of membrane to deformations. In cells, membrane tension is thought to be a combination of in-plane tension and adhesion between the membrane and underlying actin cytoskeleton.[1,2] It has been proposed that membrane tension guides shape determination in motile cells by relaying actin-based protrusive forces at the front to the disassembly and contraction of the rear.[1,3–14] Conversely, the retraction of the trailing edge appears to modulate actin organization at the cell front through propagated membrane tension changes.[15] Long-range membrane tension propagation may similarly enable protrusions to communicate with one another for the winner-take-all competition that establishes the axis of cell movement.[16–19] Membrane tension is thought to serve as a central regulator in many other facets of cell and tissue physiologies, including cell spreading and membrane trafficking,[11,20–25] immune response,[26,27] cell fate,[28,29] cell division,[30] and organ homeostasis.[31–33]

To operate as a long-range integrator of cell shape and movement, membrane tension needs to propagate rapidly and efficiently across the cell. However, the actin cortex's attachment to the plasma membrane appears to inhibit membrane flow and tension propagation when external forces are applied to the plasma membrane.[26,34–36] It remains a source of significant debate as to whether cell membranes support or resist long-range membrane tension propagation. This is a crucial point to resolve for understanding the role of membrane tension as a global integrator of cell shape and movement.

Several factors could potentially underlie the discrepancies among these conflicting studies of membrane tension propagation. For instance, tension propagation could be cell-type dependent, perhaps more efficient in migrating cells than in

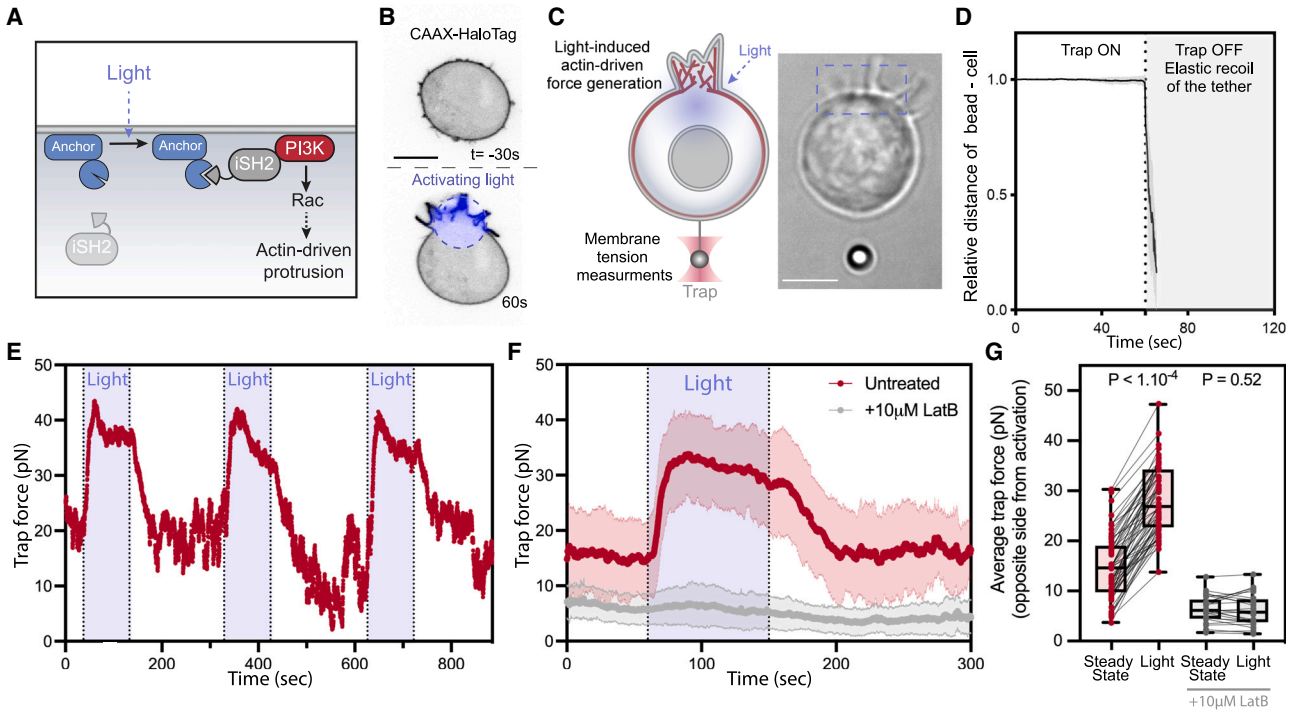

Figure 1. Local cell protrusions elicit a sharp increase in membrane tension on the opposite side of the cell within seconds

(A) Optogenetic control for light-induced activation of phosphoinositide 3-kinase (PI3K) via localized recruitment of inter SH2 domain (iSH2), resulting in Rac GTPase activation that initiates actin-driven cell protrusions (see STAR Methods).

(B) Time-lapse confocal images of a neutrophil-like HL-60 cell expressing opto-construct (Opto-PI3K) and membrane marker (CAAX-HaloTag), showing localized membrane protrusion upon light activation.

(C) After light-activated protrusion on one side of the cell (top of frame), changes in membrane tension on the opposite side (bottom of frame) are measured via a membrane tether held by an optical trap. (Right) Brightfield image of a protruding cell during tether pulling assay.

(D) After tether pulling measurements, the trapping laser is turned off, and the elastic recoil of the bead toward the cell is observed to confirm the absence of cytoskeleton in the tether (means ± SD; n > 15, N = 5).

(E) Representative time trace of trap force (a direct readout of cell membrane tension change) reveals robust and sharp increase in membrane tension over repeating cycles of light-activated protrusion on the opposite end of the cell (as in C); light: 90 s on (shaded area).

(F) Red: averaged time trace of trap force before (steady state), during (light), and after activating cell protrusion (means ± SD; n > 60, N = 8). Gray: as a control, averaged trace from cells treated with actin polymerization inhibitor (10 μM latrunculin B) shows little membrane tension change upon optogenetic activation.

(G) Averaged trap force before (steady state) and during activation. Box and whiskers: median and min to max; p values from Wilcoxon paired Student's t test. Scale bars: 5 μm. See also Figure S1 and Video S1.

non-motile cells.[35,37,38] Alternatively, the origin of discrepancies could stem from the limitations of traditional tools for manipulating and analyzing membrane tension. For example, exogenously applied mechanical perturbations of the plasma membrane may elicit tension responses that are different from those elicited by the endogenously generated mechanical forces that are exerted during cell migration. To overcome these limitations, we implemented optogenetics to control localized actin-based cell protrusions or actomyosin contractions while simultaneously monitoring membrane tension response at multiple locations around the cell using high-precision force measurements with dual-trap optical tweezers. We find that optogenetically activated cell protrusions and actomyosin contractions both induce long-range membrane tension propagation within seconds. In contrast, perturbations affecting only the plasma membrane fail to elicit membrane tension propagation—consistent with previous results.[34,35,37] We propose a simple unifying mechanical model in which the cortex resists membrane flow when forces are applied to the plasma membrane alone. In contrast, when forces engage the cortex, the membrane and cortex act as an integrated system to efficiently transmit membrane tension throughout the cell. Our work demonstrates that membrane tension has the properties expected of a long-range integrator of cell physiology, critical for its role in regulating cell shape and movement.

RESULTS

Local cell protrusions elicit a rapid long-range increase in membrane tension

To investigate membrane tension propagation upon endogenous force generation, we used an optogenetic approach (Opto-PI3K)[39,40] to activate localized actin-driven membrane protrusions in neutrophil-like HL-60 cells (Figures 1A, 1B, and S1A–S1E; Video S1) and increase membrane tension at the protruding site.[9,16,41] The propagation of membrane tension can be

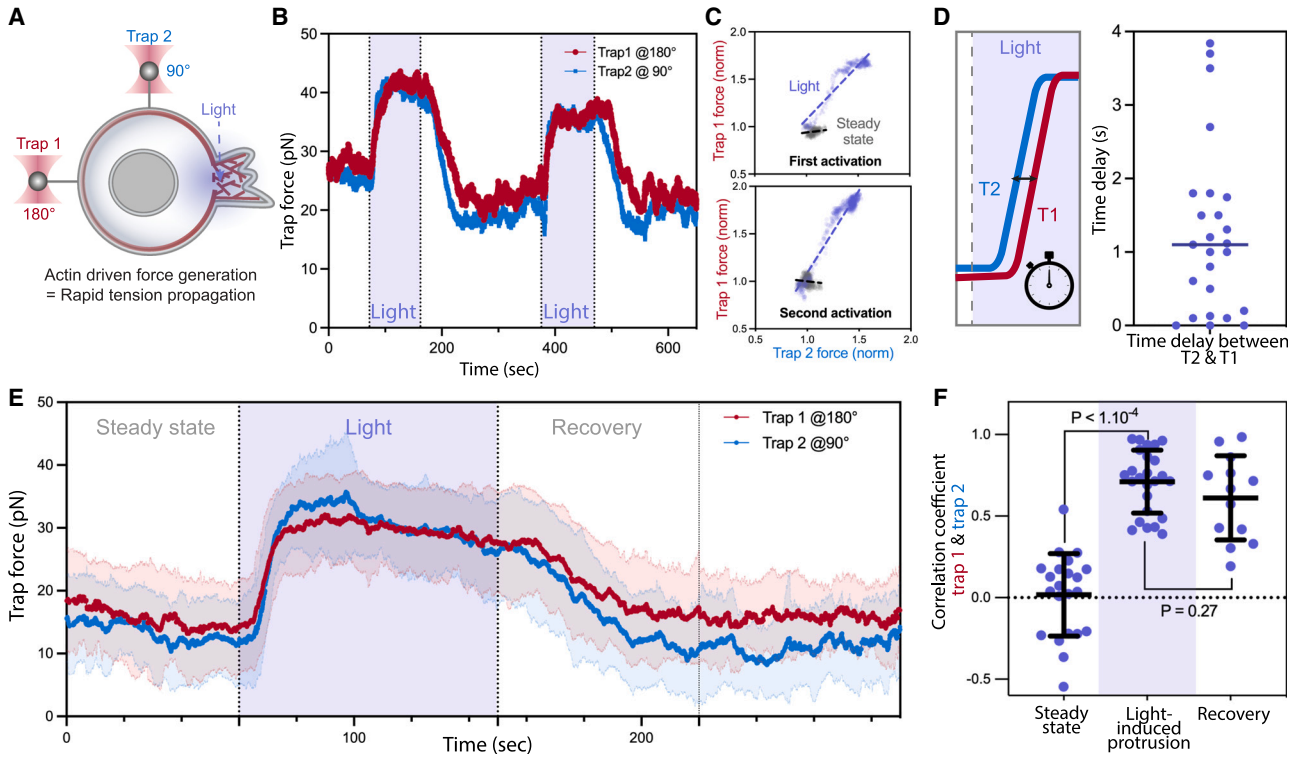

Figure 2. Actin-driven protrusions stimulate global, nearly undampened membrane tension propagation

(A) A dual-tether pulling assay to simultaneously monitor membrane tension on the far end (left, trap 1 at 180°) and on the side of the cell (top, trap 2 at 90°) during light-activated protrusion.

(B) Representative time traces of dual trap forces over successive cycles of light-activated protrusion show coinciding tension increases on both membrane tethers adjacent to (trap 2) and at the opposite cell surface from (trap 1) protrusion; light: 90 s on (shaded area), 180 s off.

(C) Correlation between trap forces at the two tether positions during activation (blue) remains robust from first activation cycle to the next; for comparison, minimal correlation is seen between the two tethers before optogenetic activation (gray). Dashed line: linear regression.

(D) (Left) Time delay measured between tension rise on membrane tethers adjacent to (trap 2 at 90°, blue) and opposite from (trap 1 at 180°, red) cell protrusion. (Right) In most cells, the traps detect membrane tension increase on both tethers within a second or less of one another, indicating a rapid propagation of tension across the cell.

(E) Averaged traces of dual trap forces before, during (light), and after activation (means ± SD; n > 25, N = 4).

(F) Pearson correlation coefficient between dual trap forces measured at steady state, during light activation, and recovery afterward (70 s post light). Error bar: means ± SD; p values from Welch's unpaired Student's t test (n > 10, N > 4). See also Figure S2 and Video S2.

probed via a membrane tether pulled out on the opposite side of cell body using a bead (coated with lectin to bind carbohydrate groups on the membrane) and held by an optical trap (a.k.a. trap-based tether pulling assay; Figure 1C; see STAR Methods). To verify that our optical trap experiments measure the forces exerted by the plasma membrane as opposed to potential actin polymerization within or along the membrane tether,[42,43] we ensured that the trapped beads linked to a membrane tether snap back to the cell within seconds upon the release of the optical trap at the end of our experimental measurements (Figure 1D; Video S1; this was a standard control in our operation protocol for all sets of optical trap experiments; see STAR Methods). In response to light-induced actin-driven protrusions, we observed a rapid long-range increase in membrane tension (Figures 1E, 1F, and S1F–S1K; Video S2). The long-range rise in tension within ~5–15 s of light activation is in stark contrast to the conclusion arrived at in recent studies[34] that "cell membranes resist flow." We also verified that the observed increase in tension correlates with the local activation of the actin regulator, Rac GTPase, which is downstream of phosphoinositide 3-kinase (PI3K) activation and precedes actin-driven protrusion (Figures S1A–S1E). As an additional control, we treated the cells with the actin inhibitor latrunculin B and observed a lack of membrane tension increase after light activation (Figures 1F, 1G, and S1L). These results demonstrate that actin-based protrusions elicit a rapid long-range propagation of membrane tension.

Actin-driven protrusions stimulate global, unattenuated membrane tension propagation

To examine the dynamics of membrane tension propagation in more detail, we performed a dual-tether pulling assay and simultaneously monitored membrane tension on the side and back of the cell (at 90° and 180° from the site of illumination, respectively) throughout multiple cycles of light-induced protrusion (Figures 2A–2C and S2; Video S2). Interestingly, the two membrane tethers exhibit a near-simultaneous increase in

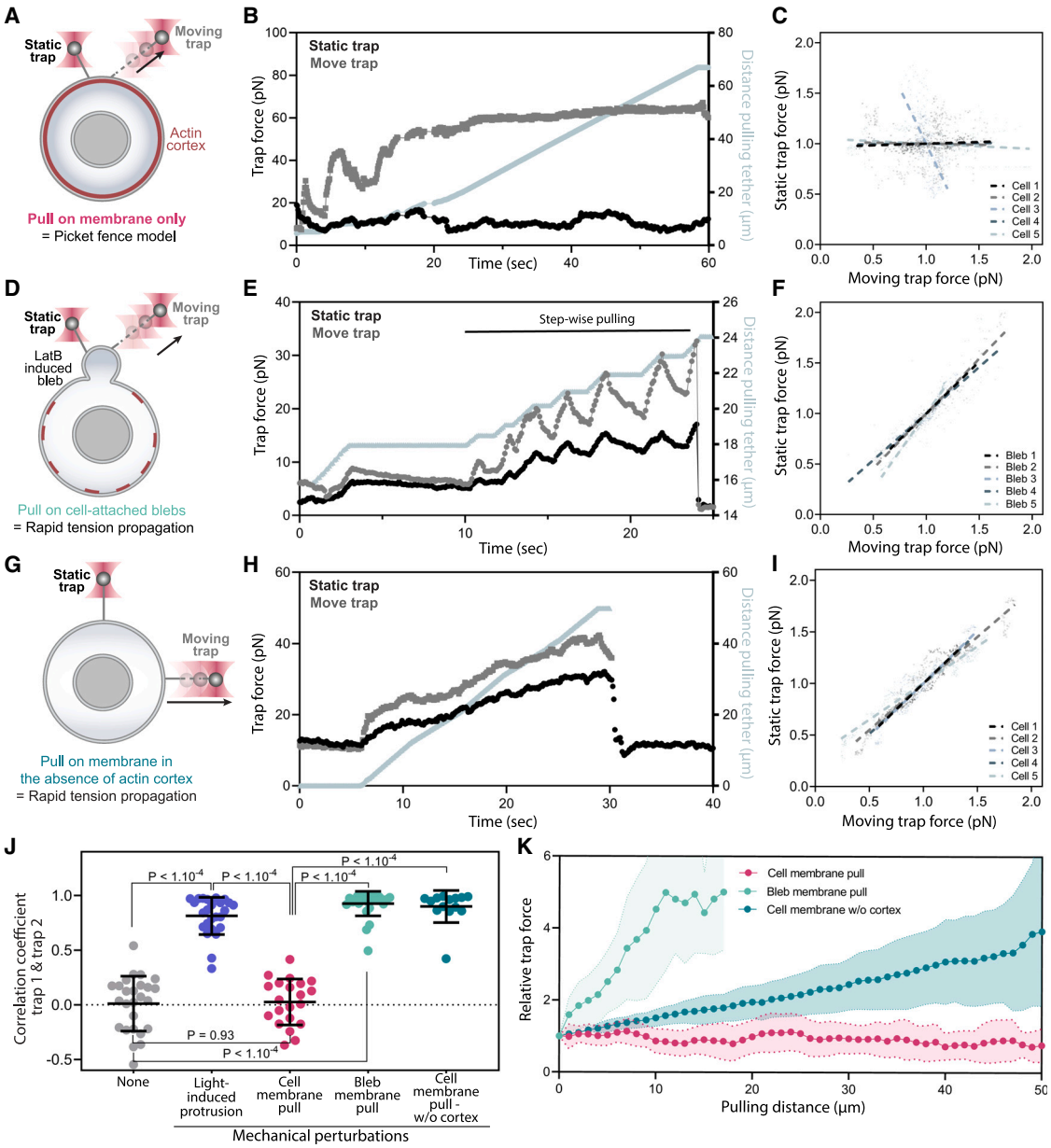

Figure 3. Membrane tension does not propagate upon direct mechanical pulling on the cell membrane

(A) A dual-tether assay to detect tension propagation (static tether, left) while a nearby force is exerted through the use of an optically trapped bead to pull on the membrane ~2-µm away (moving tether, right).

(B) An example time trace of trap force for dual membrane tension measurements, in which one moving trap (T2, gray) dynamically pulls on the cell membrane by continuously pulling and extending the membrane tether, whereas the other trap controls a second static membrane tether (T1, black) to monitor nearby changes in membrane tension. The increase in the length of the extending tether from the cell body is plotted in gray along the right y axis.

(C) Correlation plots of normalized trap forces between the moving and static tethers. Five representative measurements from different cells are shown; dashed lines: linear regression.

(D–F) Similar to (A–C), but probing tension in blebs (membrane detached from actin cortex generated by using latrunculin B treatment to weaken the actin cortex); here, a high correlation is observed between static and moving tethers.

(G–I) Similar to (A–C), but probing tension in cells where the actin cortex has been significantly disassembled using a combination of latrunculin B treatment and osmotic shock; a high correlation is observed between static and moving tethers even at a significant distance from one another (here, 90°, but in Figures S3H–S3J, 180°).

(J) Pearson correlation coefficient between dual trap forces measured before perturbations (none; light gray), upon light-activated protrusions (purple; Figure 2), during cell membrane pulling (pink; A–C), during membrane pulling on a bleb (light green; D–F), and during cell membrane pulling in cells with heavily disassembled actin cortex (dark green; G–I). Error bar: means ± SD; p values from Welch's unpaired Student's t test (n > 15, N > 3).

(legend continued on next page)

tension, with a delay, on average, of 1.2 ± 1.2 s between the two (Figure 2D). Readouts on both tethers plateau toward similar tension levels (Figures 2B, 2E, and S2A–S2C). Furthermore, membrane tension measurements of the two tethers remain highly correlated during light-activated protrusion and during recovery (Figure 2F). Our experiments indicate that endogenous actin-based protrusions generate a long-range increase in membrane tension, which is transmitted virtually unattenuated across the cell within seconds.

The actin cortex resists membrane tension propagation when external forces are applied to the membrane alone

The contradictory observations between this study and some previous studies[34,35,37,38] may originate from how a mechanical perturbation is applied to cell membranes. Here, we optogenetically induce cellular membrane protrusion (i.e., endogenous actin driven), eliciting rapid global membrane tension propagation. In this approach, the forces of actin polymerization are potentially applied to both the cortex and the plasma membrane. In contrast, previous studies concluding that membrane tension is locally constrained by the actin cytoskeleton[34] used a pair of membrane tethers to pull on the cell membrane (i.e., exogenous bead pulling), thereby applying forces to the plasma membrane alone. To test whether the membrane-tether-induced forces also fail to propagate in our cells, we repurposed our dual-tether assay to dynamically pull one tether by actively moving the first trap while measuring membrane tension on a nearby membrane tether held in place by the second trap (i.e., Figure 2A versus Figure 3A). In line with analogous experiments performed in epithelial cells, we observe no propagation of membrane tension from the extending tether to the static one (Figures 3A–3C, 3J, 3K, S3A, and S3D; Video S2)—even with the two tethers in close proximity (<2 μm apart). In contrast, when we performed the same dual-tether assay on cellular blebs (membrane detached from actin cortex, achieved in latrunculin-treated cells), tension propagates almost instantly (<100 μs, i.e., below the temporal resolution of the optical tweezers instrument; Figures 3D–3F, 3J, 3K, S3B, S3C, S3E, and S3F; Video S2), in agreement with similar measurements in epithelial cells.[34] These bleb-based experiments can only test tension propagation at the size scale of cellular blebs (<4 μm). To test whether tension can propagate for longer distances, we performed tether experiments in cells treated with inhibitors that efficiently disassemble the actin cytoskeleton. Because latrunculin does not suffice to depolymerize a population of latrunculin-resistant actin filaments, we used a combination of latrunculin treatment and osmotic shock, which has previously been shown to adequately depolymerize the actin cortex,[44] as we verify in our cells (Figure S3G). These cortex-free cells exhibited rapid long-range propagation of membrane tension, both for traps at 90° (Figures 3G–3I) and traps at opposite ends of the cell (Figures S3H–S3J; Video S2). Both blebs and cortically depolymerized cells propagate tension when forces are applied to the plasma membrane alone, but cells with an intact cortex do not (Figures 3J and 3K). Our observations that effective membrane tension propagation depends on how mechanical perturbations are exerted within the context of the same cell type (Figures 2, 3, S2, and S3) suggest that existing disagreements in the field are at least partially methodological in nature. While mechanical perturbations via exogenous tether pulling fail to elicit membrane tension propagation (consistent with the "picket fence" model of cortex adhesion to the plasma membrane[34,38]), endogenous actin-based force generation efficiently promotes membrane tension propagation across the cell.

Long-range tension propagation coincides with directed membrane and actin flows toward the protrusion

Next, we investigated the mechanism of tension propagation from the site of protrusion to the rest of the cell. We observed the enrichment of our plasma membrane probe in the opto-induced protrusions (Figure 1B; Video S3) on a similar timescale to that of cellular deformation and tension increase (10–15 s) following optogenetic protrusion generation (Figures S1C–S1E). We hypothesized that membrane and cortical flows could underlie the rapid propagation of membrane tension from the site of protrusion to the rest of the cell. To resolve the time-dependent flow of the plasma membrane and actin cytoskeleton relative to light-activated protrusions, we used fluorescent markers of the plasma membrane (CAAX-HaloTag) and actin cytoskeleton (Actin-HaloTag); these markers were respectively examined in separate cells. During protrusion formation, the intensity of the plasma membrane probe is increased at the site of protrusion while decreasing elsewhere (Figures 4A, 4B, and S4A–S4G; Video S3). Because the true width of the plasma membrane is likely to be constant during our experiments, these apparent shifts in intensity presumably represent the bunching and unfolding of sub-resolution plasma membrane folds.[45] Neutrophils have more than twice the amount of plasma membrane needed for their apparent cell size, and this excess is held in wrinkled plasma membrane reservoirs.[46–48] The actin probe similarly accumulated at the site of protrusion and decreased on the side of the cell opposite from the protrusion (Video S3).

To characterize the flows of membrane and actin over time, we developed a novel flow inference method based on kymographs to predict a flow field that can explain the spatiotemporal redistribution of membrane (or actin) intensity (Figure 4C). A model to rationalize our experimental observations is that the protrusion resulting from the actin polymerization pulls the actin cortex toward the protrusion front, which, in turn, drags the membrane around the cell at each point to which it is connected. In this case, it is reasonable to assume that the flows resulting from the actin-driven protrusions are accompanied by dissipation generated by the friction between the membrane and its underlying cortex. Under these conditions, the observed flow reduces to a case of optimal transport[49,50], which minimizes the dissipation. Thus, it is possible to infer membrane and cortical velocity fields from the experimental kymographs using the optimal

(K) Relative force changes (y axis) for membrane tension monitored on the static tether as a function of the extending tether length (x axis) upon continuous pulling. In the case of blebs or cells with heavily disassembled actin cortex (light and dark green), the tension on static tether increases as the extending tether lengthens; however, there are no perceptible tension changes on the static tether tension from the cell body (pink, intact cortex) even when the other tether has extended by more than 60 μm (n > 14, N > 3). Graphical data represent means ± SDs. See also Figure S3 and Video S2.

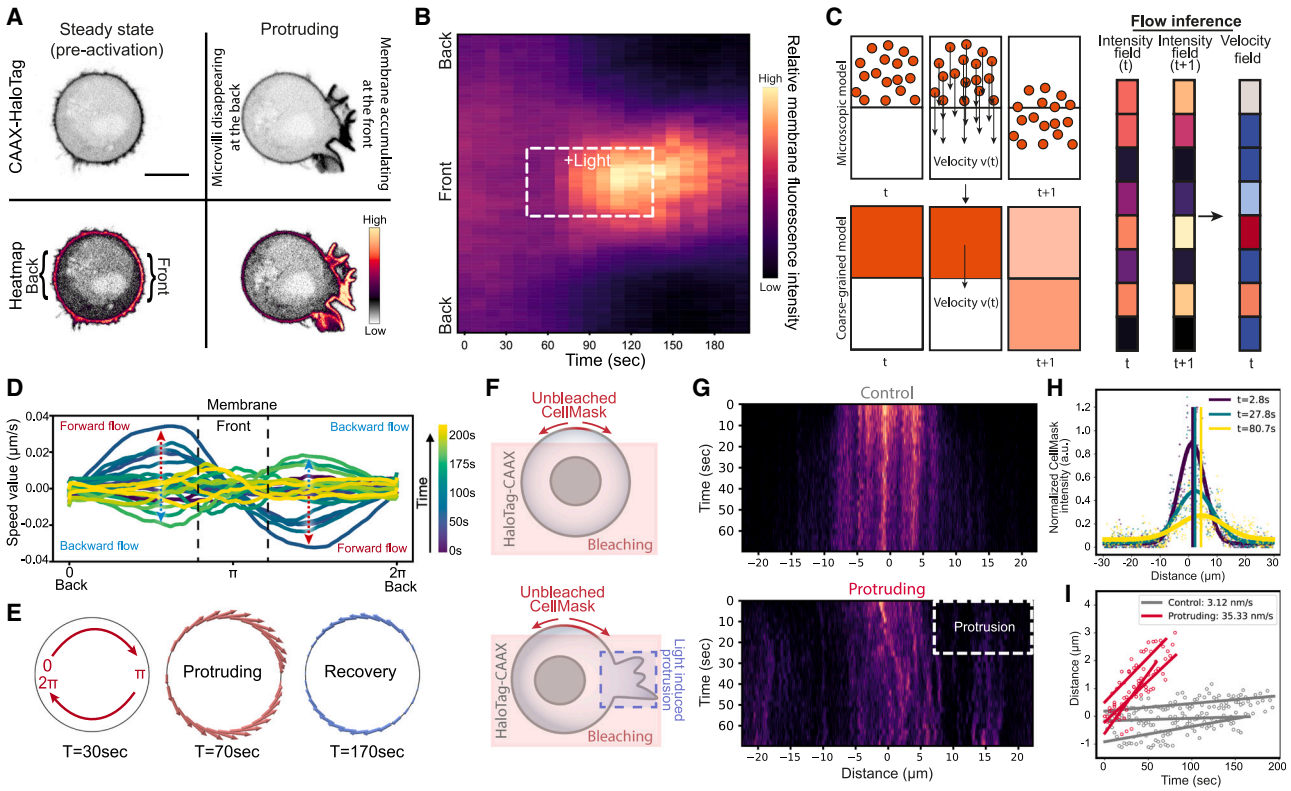

Figure 4. Long-range tension propagation is accompanied by directed membrane and actin flows toward the protrusion

(A) Confocal images of opto-PI3K cells expressing membrane marker (CAAX-HaloTag): before and during light-activated protrusion. Scale bars: 5 μm.

(B) Kymographs of membrane fluorescence along the normalized cell circumference (y axis) show that over time (x axis) membrane accumulates toward the protruding cell front and is depleted from the back (n > 50, N = 6; Figure S4; see STAR Methods).

(C) Flows of membrane and actin during protrusion are calculated assuming optimal transport (see STAR Methods).

(D) Membrane flow field inferred using optimal transport from kymograph intensity changes over time: shortly after activation begins (t = 70 s, dark teal traces), the magnitude of membrane flow speed increases (red dashed arrows), with positive speed for clockwise flow along the cell upper half and negative speed for counter-clockwise flow along the bottom half (G), all moving toward the cell protruding front (π). During recovery (t = 170 s, light green traces), the direction of membrane flow reverses (blue dashed arrows).

(E) Membrane flow around the cell before, during, and after (t = 30, 70, and 170 s) right-side protrusion; the flow magnitude is denoted by the arrow size (red: forward flow, blue: backward). Membrane flows toward the protrusion in the protruding phase and away from the protrusion during the recovery phase.

(F) Alternative membrane diffusion assay in which we bleach the membrane marker CellMask across a wide section of the cell (sparing a small section of the membrane maker), opto-activate a portion of the cell angled 90° from the unbleached area (or use no light as control), and monitor the diffusion pattern of the unbleached area over time.

(G) (Top) Example kymograph of unbiased diffusion in a control cell (no activating light). (Bottom) Same as top but in a protruding cell, showing biased diffusion and bulk flow of the unbleached membrane signal toward the protrusion. Heatmap similar as in (B).

(H) Sample fits of individual timepoints of kymograph data (points colored by respective time points) with a gaussian equation (thick curves, colored by respective time points). Shifts in the means of the gaussian fits, quantified bulk membrane flow, are shown as vertical lines (colored by respective timepoints).

(I) Quantification of mean shifts fit by linear regression to assay membrane flow rate in control cells (gray, no apparent flow, u = 3.34 nm/s) and protruding cells (red, biased flow toward side of protrusion, u = 35.51 nm/s) (N = 3, n = 3). See also Figure S4 and Video S3.

transport theory (see Methods S1; Figures S4H and S4I). We verified that our inference method is able to recover velocity fields from various simulated kymographs with high accuracy (Figure S4J; Methods S1). Our analysis revealed the presence of a cell-wide flow of both plasma membrane and actin cortex toward the protruding front during light-induced protrusion, and these flows reverse direction during recovery (Figures 4D, 4E, S4F, S4G, and S4K; Video S3). We used membrane photobleaching (Figures 4F–4I and S4L–S4P) and the tracking of microvilli movement (Figure S4Q; Video S3) to further validate plasma membrane flows toward the protrusion. These directed membrane and cortex flows provide a potential mechanism to mediate tension propagation upon cell protrusion.

Actomyosin contractions also generate rapid long-range membrane tension propagation and membrane flows

Because actin-based protrusions elicit membrane and actin flows (Figure 4; Video S3) that mediate tension propagation (Figures 1 and 2; Video S2), but forces applied to the membrane alone do not (Figures 3 and S3; Video S2), our data suggest that forces applied to the actin cortex could be central to

membrane tension propagation. As optogenetically activated protrusions exert forces on both the cortex and plasma membrane, we next sought to investigate the consequences of applying forces directly to the actin cortex. For this purpose, we leveraged an optogenetic approach to induce local actomyosin contractility through the local recruitment of the Rho-activating domain of LARG (leukemia-associated *Rho* guanine nucleotide exchange factor) (Figures 5A–5C).[51] Focal Rho activation elicited the local flattening of the cell (Figure 5B), as expected from local myosin activation.[52,53] Similar to light-activated protrusions (Figures 1 and 2), light-activated actomyosin contractility also generated a long-range transmission of membrane tension (Figure 5D and 5E) that rapidly propagated virtually unattenuated across the cell (Figures 5F–5H). As we observed for actin-based protrusions, the local generation of actomyosin contractility also generated flows of both plasma membrane (Figures 5I–5L; Video S4) and actin cortex (Figures S5E–S5H; Video S4) toward the site of contractions. As an additional control, we also used the speckle tracking of focal enrichments of the actin cortex to demonstrate cortical flows toward the site of contractions (Figure S5I; Video S4). These data suggest that forces applied to the actin cortex are sufficient for efficient membrane flows and membrane tension propagation in cells

Mechanical forces engaging the actin cortex drive robust membrane tension propagation in cells

To infer the critical requirements for cellular membrane tension propagation, we constructed a simple composite mechanical model in which an elastic plasma membrane is coupled to a viscous and contractile gel-like actomyosin cortex[52] via adhesive linkers (Figure 6A; see Methods S1). The tension of a 2D membrane is overall of an entropic origin and corresponds to the unfolding of membrane fluctuations. In such entropic regime, membrane tension is proportional to the exponential of the area strain, as found experimentally[54] and predicted theoretically.[55] Our model assumes small strains, where this exponential behaves approximately as an affine function and where the membrane can be considered as linearly elastic.

For the simplicity of our model, we neglected the contribution of membrane reservoirs, as we do not envision that these dominate tension propagation. The presence of multiple membrane reservoirs that can unfold above a given tension threshold would simply limit the ability of tension to increase above this value. Our experimental data are consistent with reservoirs being accessed at the plateau phase (maximum tension values) of tension propagation. At early, pre-plateau phases of protrusion extension, membrane tension increases rapidly even for relatively small protrusions and then plateaus at a maximum even as the protrusion continues to expand (Figure S1F). Neutrophils have much larger plasma membrane reservoirs than other cells such as fibroblasts (Figures S6A and S6B[56]), making it unlikely that we are exhausting local reservoirs during early, pre-plateau phases of protrusion/contraction or during our tether pulling experiments. Intriguingly, both optogenetically induced protrusions and optogenetically induced contractions reach similar maximal membrane tension values, likely reflecting the threshold of accessing membrane tension buffers (Figures 2 and 5). Therefore, membrane tension propagation observed in the pre-plateau phases—the focus of our study here—is unlikely to be affected by the presence of folded membrane reservoirs as tension buffers, which manifest mostly in the plateau phase.

In our model, the membrane displacement (x_i)—upon cortical flows (v_i)—is determined by the overall friction imposed through the interconnecting layer of adhesive linkers (e.g., membrane-to-cortex attachment proteins [MCAs], such as Ezrin). This friction μ exerts a drag force on the cell membrane with a magnitude that is proportional to the relative tangential velocity between the cortex and membrane. Given a moderate membrane-cortex friction, this model adequately captures the known tension responses upon different types of mechanical perturbations (Figures 6B and 6C), including the absence of tension transmission when only the membrane is pulled (e.g., exogenous tether pulling) and rapid propagation of tension upon actin-based cell contraction/protrusion (e.g., endogenous force generation). Furthermore, the model suggests that perturbations engaging both membrane and cortex not only lead to tension propagation but also exhibit a robust tension transmission over a much wider range of membrane-cortex coupling conditions than perturbations engaging either component alone. To test how membrane tension propagation is affected by weakening MCA, we utilized NSC668394, an inhibitor of Ezrin phosphorylation and Ezrin-actin binding. In accordance with the predictions of our model (Figure 6C), this Ezrin inhibitor elicited only mild defects in protrusion-mediated tension propagation (Figures 6D, 6E, and S6C) and elicited more significant defects in contraction-mediated tension propagation (Figures 6F, 6G, and S6C).

Our modeling suggests that the key determinant of long-range membrane response is not the endogenous or exogenous application of force but rather whether the mechanical forces directly engage the actin cortex and whether the cortex is sufficiently attached to the membrane (i.e., sufficient friction/coupling) to effectively transmit forces to produce membrane displacement upon cortex displacement. To test whether exogenously applied forces can mediate membrane tension propagation, we implemented micropipette aspiration to apply mechanical pulling on both the actin cortex and plasma membrane and monitored tension propagation using our dual-tether assay (Figure 6H; see STAR Methods). We detected a rapid, robust, and global increase in membrane tension with little to no attenuation across the cell (Figures 6I, 6J, and S6D–S6L; Video S5). Our unifying model indicates that the plasma membrane and actin cortex act as an integrated system for robust membrane tension propagation.

DISCUSSION

By combining optogenetics for local endogenous control of cell protrusion/contraction and optical trapping for direct membrane tension measurements in tether pulling assays, we demonstrate that local mechanical force generation such as through cellular protrusions and contractions elicits rapid long-range propagation of membrane tension throughout the cell. In addition, our findings resolve the long-standing dispute as to whether the actin cortex facilitates or impedes tension propagation. When forces are applied to membranes alone (e.g., tether pulling), the actin cortex opposes membrane flow and tension

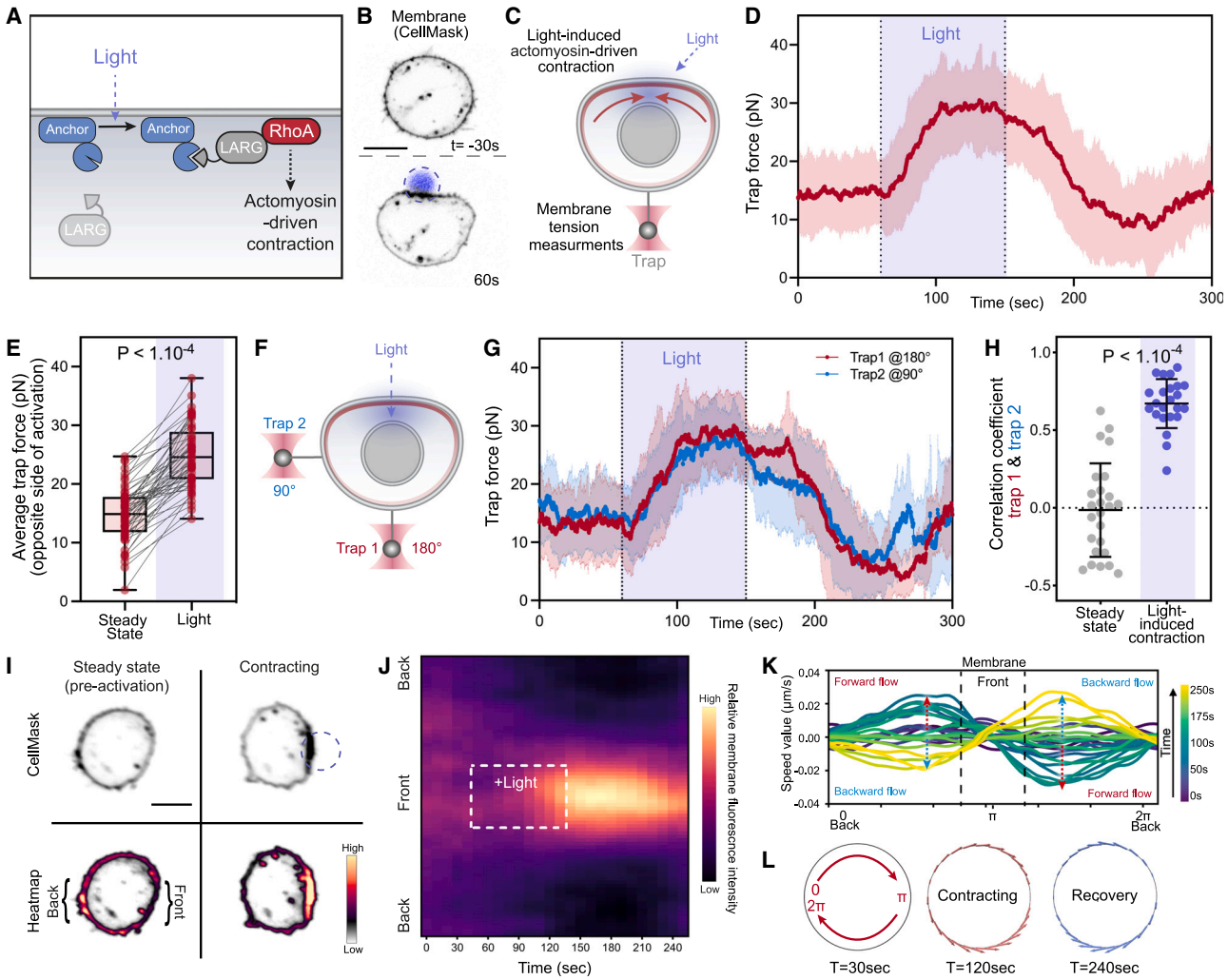

Figure 5. Optogenetically induced actomyosin contractions generate rapid long-range membrane tension propagation and membrane flows

(A) Optogenetic approach for light-induced activation of leukemia-associated Rho guanine nucleotide exchange factor (LARG), resulting in Rho GTPase activation to initiate actomyosin-driven cell contraction (see STAR Methods).

(B) Time-lapse confocal images of a neutrophil-like HL-60 cell expressing opto-construct (Opto-LARG) and membrane marker (CellMask), showing localized membrane contraction and cell flattening upon light activation.

(C) After light-activated contraction on one side of the cell (top), changes in membrane tension on the opposite side (bottom) are measured via a membrane tether held by an optical trap.

(D) Averaged time trace of trap force before (steady state), during (light), and after activating cell contraction (means ± SD; n > 55, N = 7).

(E) Averaged trap force before (steady state) and during activation. Box and whiskers: median and min to max; p values from Wilcoxon paired Student's t test.

(F) A dual-tether pulling assay to simultaneously monitor membrane tension on the far end (left, trap 1 at 180°) and on the side of the cell (top, trap 2 at 90°) during light-activated contraction.

(G) Averaged traces of dual trap forces before, during (light), and after activation showing coinciding tension increases on both membrane tethers adjacent to (trap 2) and at the opposite cell surface from (trap 1) contraction (means ± SD; n = 25, N = 4).

(H) Pearson correlation coefficient between dual trap forces measured at steady state and during light activation. Error bar: means ± SD; p values from Welch's unpaired Student's t test (n > 20, N > 4).

(I) Confocal images of opto-LARG cells stained with membrane marker (CellMask) before and during light-activated contraction.

(J) Kymographs of membrane fluorescence along the normalized cell circumference (y axis) show that over time (x axis) membrane accumulates toward the contracting cell front and is depleted from the back (n = 40, N = 3; see STAR Methods).

(K) Membrane flow field inferred using optimal transport from kymograph intensity changes over time: shortly after activation begins (t = 120 s, teal traces), the magnitude of membrane flow speed increases (red dashed arrows), with positive speed for clockwise flow along the cell upper half and negative speed for counter-clockwise flow along the bottom half, all moving toward the site of cell contraction (π). During recovery (t = 200 s, light green traces), the direction of membrane flow reverses (blue dashed arrows).

(L) Membrane flow around the cell before, during, and after (t = 30, 120, and 240 s) right-side contraction; the flow magnitude is denoted by the arrow size (red: forward flow, blue: backward). Membrane flows toward the contraction in the contracting phase and away from the contraction during the recovery phase. Scale bars: 5 μm. See also Figure S5 and Video S4.

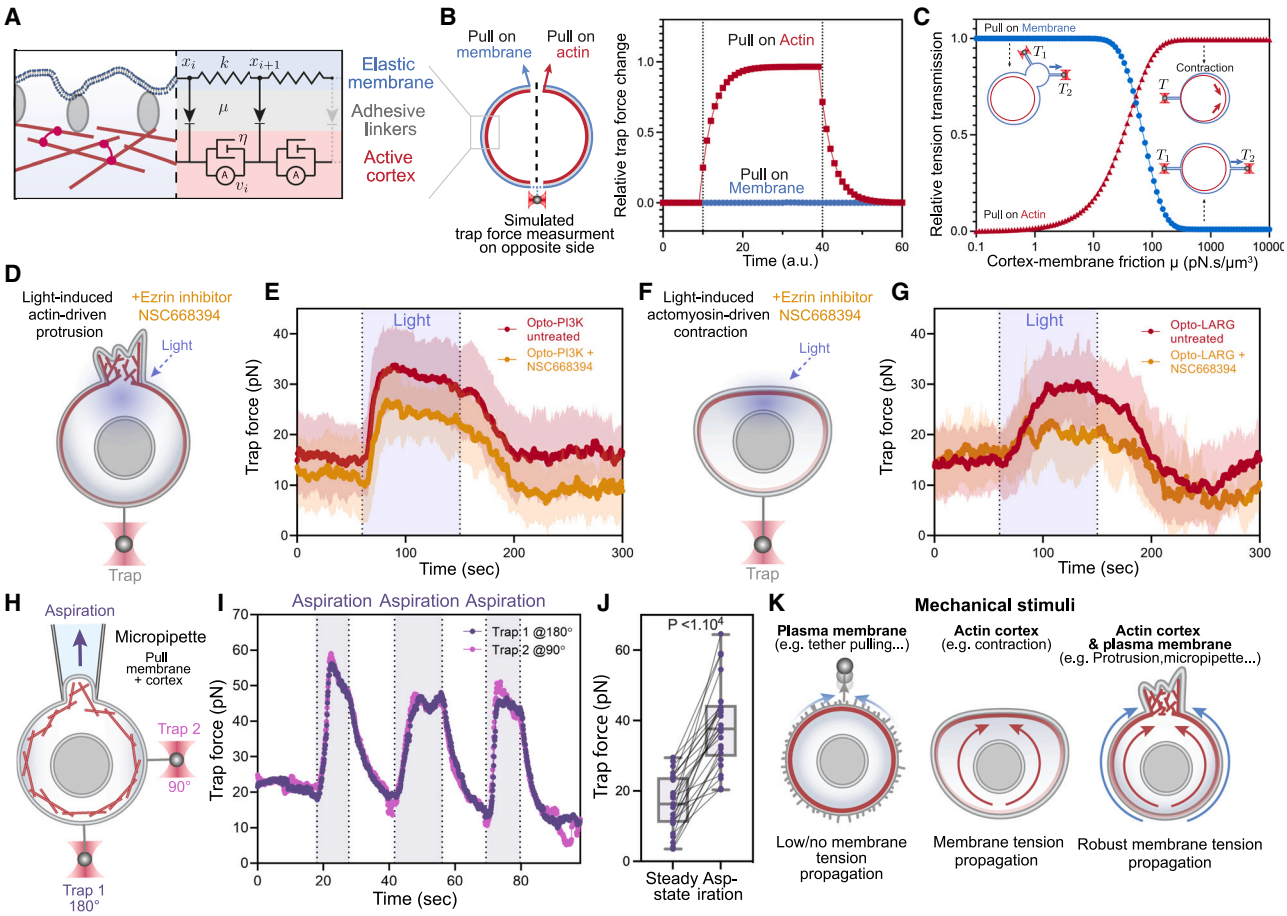

Figure 6. Mechanical forces acting on the actin cortex drive rapid long-range membrane tension propagation in cells

(A) A 3-tier composite model for membrane tension propagation in cells: membrane displacements (x_i) as a readout for tension propagation upon cortical flows (v_i) depend on the membrane elasticity (k) and the membrane-cortex friction μ imposed through the adhesive linkers.

(B) Model predictions of membrane tension response at moderate membrane-cortex friction (see Methods S1): only actin-based pulling leads to tension increase and propagation (red rectangles); external pulling on the membrane alone is inefficient (blue circles).

(C) Predicted membrane tension transmission as a function of membrane-cortex friction (x axis) for different targets of force application: plasma membrane only (blue) and actin cortex only (red).

(D) Membrane tension measurements during light-induced protrusions in cells with decreased MCA by using 25 μM of Ezrin inhibitor NSC668394.

(E) Red: averaged time trace of trap force before (steady state), during (light) and after activating cell protrusion in control cells (same data as Figure 1F). Orange: averaged trace from cells with decreased MCA by using 25 μM of Ezrin inhibitor NSC668394, showing slight defects in membrane tension propagation during light-activated protrusions (means ± SD; n > 25, N = 3).

(F and G) Similar to (D and E) but using light-induced actomyosin contractions, in which decreases in MCA lead to severe defects in membrane tension propagation across the cell (red: same data as Figure 5D; means ± SD; n > 25, N = 4).

(H) A dual-tether assay to simultaneously monitor membrane tension on the far end (bottom, trap 1 at 180°) and on the side of the cell (right, trap 2 at 90°) during micropipette aspiration (top), which mechanically pulls on both the membrane and underlying actin cortex (see STAR Methods).

(I) Representative time traces of dual trap forces over successive cycles of aspiration (shaded area) show coinciding tension increases and decreases on both membrane tethers, similar to that in Figure 2B.

(J) Averaged trap forces measured before (steady state) and during aspiration. The robust increase in membrane tension upon aspiration of both membrane and cortex is consistent with our model prediction (B). Box and whiskers: median and min to max; p values from Wilcoxon paired Student's t test (n > 25, N = 5).

(K) Schematic of requirements for effective membrane tension propagation: in the presence of membrane-to-cortex attachments, force application to plasma membrane alone does not generate tension propagation, in agreement with the picket fence model. However, mechanical stimuli acting on actin cortex, such as contraction, lead to rapid, long-range membrane tension propagation in the presence of significant membrane-to-cortex attachments. Perturbations affecting both actin cortex and plasma membrane (such as protrusions or micropipette aspiration) lead to robust long-range membrane tension propagation regardless of membrane-to-cortex attachment levels. See also Figure S6, Methods S1, and Video S5.

propagation. However, when forces engage the actin cortex underneath the membrane—either upon optogenetically induced actin polymerization or actomyosin contraction or upon micropipette aspiration—tension rapidly propagates nearly undampened across the cell through the generation of actin-driven membrane flows (Figure 6K).

It is noteworthy that the propagation of membrane tension after cell protrusion/contraction is not only rapid but also unattenuated, an optimal behavior for coordinating processes at the scale of the entire cell. Our experiments and modeling suggest that one essential prerequisite for this efficient tension propagation is that the force transmits through the cortex. Accordingly, we propose that the cortical propagation of tension across the cell is supported by a continuous cortical network and that interactions between the cortex and cellular substrates other than the low-stiffness, highly compliant plasma membrane must be sufficiently weak so as to minimize dissipative losses in tension propagation. Any discontinuities in the cortex or physical barriers that disrupt cortical flow (e.g., the division between the apical versus basolateral portions of epithelia cells) would be expected to impede tension propagation. Consistent with this idea, we observe more robust membrane flows toward the protrusion for the portions of the cell away from the substrate surface compared with the substrate-adhered ventral region of the cell (Figures S6M–S6P).

Actin-based protrusions and actomyosin contractions both mediate long-range membrane tension propagation and flows of both actin and membrane toward the site of protrusion/contraction (Figures 4, 5, S4, and S5). For actomyosin contraction, the primary force is the myosin contractility that generates the actin flows. In this case, the flow of the plasma membrane and propagation of membrane tension depend on high MCA (Figures 6C, 6F, and 6G). Compared with actomyosin contraction, we have less of an understanding of why the cortex flows toward the protrusion. We speculate that the newly polymerized actin at the leading edge generates a pushing force on the membrane while also generating a pulling force on the preexisting actin cortex. Future high-resolution electron microscopy images of protrusive and cortical actin could help reveal the relative organization of these actin networks during motility.[15,57]

Our modeling suggests that forces that engage both the cortex and plasma membrane could ensure robust membrane tension propagation over a wide range of membrane-to-cortex adhesion strengths (Figures 6C–6E). During light-activated cell protrusions, forces from actin polymerization are exerted on both the plasma membrane and actin cortex, as can be observed by the flow of membrane and cortex toward the site of protrusion (Figure 4). Membrane flows enable membrane tension propagation in regions of low MCA, cortical flows permit membrane tension propagation in areas of high MCA, and forces applied to both networks should propagate tension in both settings. The ability of protrusions to engage both the plasma membrane and cortex may be particularly important for long-range tension propagation in motile cells with discontinuous MCAs.[58] We envision that actin polymerization at the leading edge, where the attachment between the cortex and plasma membrane is weak[58,59], would extend the plasma membrane perpendicular to actin cortex and cause the plasma membrane to flow toward the protrusion, whereas at the periphery of the cells (where MCA goes back up), membrane tension would be propagated via pulling forces from the actin cortex.

Our work indicates that membrane tension has the properties expected of a long-range integrator of cell physiology. Long-range propagation of membrane tension could mediate the competition among multiple protrusion sites for a "winner-take-all" establishment of a dominant front[16,18,60] and could enable the front-back coordination that maintains cell shape and movement.[5,7,9,14,15] In contrast, the coordination of cellular processes that do not apply significant forces to actin cortex may be more dependent on local membrane reservoirs; this property could explain why filopodia can coexist in adjacent regions of the cell without substantially affecting one another.[61,62] In future work, it will be critical to examine how cells modulate the dynamic range of membrane tension propagation based on the origin of the forces as well as the continuity and mechanical properties of the cortex.

Limitations of the study

In this study, we leverage multiple modes of force generation (optogenetic protrusion formation, optogenetic cell contractility, optical-trap-based tether pulling, and micropipette aspiration) to probe the requirements for membrane tension propagation in cells. Our model system for this work is neutrophil-like HL-60 cells. The mechanical model we propose explains our experimental results, correctly predicts the effects of MCA perturbations, and is consistent with both our experimental observations and those from other groups. Therefore, our general conclusions on membrane tension propagation are likely to translate to other cellular settings. However, it is likely that some of the quantitative features we observe in our cells, in particular, the nearly unattenuated propagation of tension across the cell and the precise speed of tension propagation, may differ in other cells where the cortex has different mechanical properties or where there is active mechanosensory-based regulation of the membrane or cortex. Therefore, it will be important to extend our approach—in particular, the optogenetic engagement of endogenous membrane/cortex forces and direct measurement of membrane tension propagation—to a broader diversity of cell types.

STAR★METHODS

Detailed methods are provided in the online version of this paper and include the following:

- KEY RESOURCES TABLE
- RESOURCE AVAILABILITY
  - Lead contact
  - Materials availability
  - Data and code availability
- EXPERIMENTAL MODEL AND SUBJECT DETAILS
- METHOD DETAILS
  - Transduction of HL-60 cells
  - Microscopy hardware
  - Preparation of Opto-PI3K and Opto-LARG cells for confocal imaging
  - Preparation, settings, and operation procedures for membrane tethering pulling experiments on C-trap® optical tweezers with confocal imaging
  - Optical trapping – setting and operations
  - Micropipette aspiration
- QUANTIFICATION AND STATISTICAL ANALYSIS
  - Image and membrane tension analysis

- Statistical analysis

SUPPLEMENTAL INFORMATION

Supplemental information can be found online at https://doi.org/10.1016/j.cell.2023.05.014.

ACKNOWLEDGMENTS

The authors thank M. Wu for kindly sharing plasmids and reagents and Prof. S. X. Liu for careful reading and comments on our manuscript. They thank all present and past members of the Weiner, Turlier, and Bustamante labs for critical discussions. They also thank the support from Lumicks on C-trap application in live cell studies, specifically Drs. S. Leachman, N. Hadizadeh, H. Kelkar, and J. Janmaat for technical assistance in instrumentation and Drs. E. Lissek, W. Peutz, M. Johnson, and P. Wheeler for support with operational sustainability. Data for this study were acquired at the Center for Advanced Light Microscopy-Nikon Imaging Center at UCSF on instruments obtained using grants from the UCSF Program for Breakthrough Biomedical Research funded in part by the Sandler Foundation, the Strategic Advisory Committee, and the EVCP Office Research Resource Program Institutional Matching Instrumentation Award. This work was funded by The National Institutes of Health grant GM118167 (O.D.W.); the National Science Foundation/Biotechnology and Biological Sciences Research Council grant 2019598 (O.D.W.); the National Science Foundation Center for Cellular Construction grant DBI-1548297 (O.D.W.); a Novo Nordisk Foundation grant for the Center for Geometrically Engineered Cellular Systems, NNF17OC0028176 (O.D.W.); the Labex MemoLife, France under the program ''Investissements d'Avenir'' ANR-10-LABX-54 (H.B.d.R.); the European Research Council (ERC) under the European Union's Horizon 2020 research and innovation programme, grant agreement no. 949267 (H.B.d.R. and H.T.); a QLife (ANR-17-CONV-0005)/QBio grant (O.D.W. and H.T.); EMBO ALTF 203-2021 (H.D.B.) and T32EB009383 (P.J.Z.); an American Heart Association Postdoctoral Fellowship (K.M.); the National Institutes of Health grant K99GM137074 (S.Y.); and the Howard Hughes Medical Institute (C.B.).

AUTHOR CONTRIBUTIONS

Conceptualization, O.D.W., H.D.B., and S.Y.; Methodology, H.D.B., S.Y., O.D.W., H.T., J.T., S.I., H.B.d.R., P.J.Z., D.C.E., and K.M.; Investigation, H.D.B., S.Y., S.I., and H.B.d.R.; Visualization, H.D.B. and S.Y.; Funding acquisition, O.D.W., H.T., H.D.B., H.B.d.R., S.Y., and C.B.; Supervision, O.D.W., C.B., and H.T.; Writing, H.D.B., S.Y., O.D.W., C.B., and H.T.

DECLARATION OF INTERESTS

The authors declare no competing interests.

INCLUSION AND DIVERSITY

We support inclusive, diverse, and equitable conduct of research.

Received: October 17, 2022
Revised: March 10, 2023
Accepted: May 11, 2023
Published: June 12, 2023

REFERENCES

1. Pontes, B., Monzo, P., Gole, L., Le Roux, A.-L., Kosmalska, A.J., Tam, Z.Y., Luo, W., Kan, S., Viasnoff, V., Roca-Cusachs, P., et al. (2017). Membrane tension controls adhesion positioning at the leading edge of cells. J. Cell Biol. *216*, 2959–2977. https://doi.org/10.1083/jcb.201611117.
2. Sitarska, E., and Diz-Muñoz, A. (2020). Pay attention to membrane tension: mechanobiology of the cell surface. Curr. Opin. Cell Biol. *66*, 11–18. https://doi.org/10.1016/j.ceb.2020.04.001.
3. Batchelder, E.L., Hollopeter, G., Campillo, C., Mezanges, X., Jorgensen, E.M., Nassoy, P., Sens, P., and Plastino, J. (2011). Membrane tension regulates motility by controlling lamellipodium organization. Proc. Natl. Acad. Sci. USA *108*, 11429–11434. https://doi.org/10.1073/pnas.1010481108.
4. Fogelson, B., and Mogilner, A. (2014). Computational estimates of membrane flow and tension gradient in motile cells. PLoS One *9*, e84524. https://doi.org/10.1371/journal.pone.0084524.
5. Hetmanski, J.H.R., de Belly, H., Busnelli, I., Waring, T., Nair, R.V., Sokleva, V., Dobre, O., Cameron, A., Gauthier, N., Lamaze, C., et al. (2019). Membrane tension orchestrates rear retraction in matrix-directed cell migration. Dev. Cell *51*, 460–475.e10. https://doi.org/10.1016/j.devcel.2019.09.006.
6. Kapustina, M., Elston, T.C., and Jacobson, K. (2013). Compression and dilation of the membrane-cortex layer generates rapid changes in cell shape. J. Cell Biol. *200*, 95–108. https://doi.org/10.1083/jcb.201204157.
7. Keren, K., Pincus, Z., Allen, G.M., Barnhart, E.L., Marriott, G., Mogilner, A., and Theriot, J.A. (2008). Mechanism of shape determination in motile cells. Nature *453*, 475–480. https://doi.org/10.1038/nature06952.
8. Lavi, I., Goudarzi, M., Raz, E., Gov, N.S., Voituriez, R., and Sens, P. (2019). Cellular blebs and membrane invaginations are coupled through membrane tension buffering. Biophys. J. *117*, 1485–1495. https://doi.org/10.1016/j.bpj.2019.08.002.
9. Lieber, A.D., Yehudai-Resheff, S., Barnhart, E.L., Theriot, J.A., and Keren, K. (2013). Membrane tension in rapidly moving cells is determined by cytoskeletal forces. Curr. Biol. *23*, 1409–1417. https://doi.org/10.1016/j.cub.2013.05.063.
10. Ofer, N., Mogilner, A., and Keren, K. (2011). Actin disassembly clock determines shape and speed of lamellipodial fragments. Proc. Natl. Acad. Sci. USA *108*, 20394–20399. https://doi.org/10.1073/pnas.1105333108.
11. Raucher, D., and Sheetz, M.P. (2000). Cell spreading and lamellipodial extension rate is regulated by membrane tension. J. Cell Biol. *148*, 127–136. https://doi.org/10.1083/jcb.148.1.127.
12. Ren, C., Yuan, Q., Braun, M., Zhang, X., Petri, B., Zhang, J., Kim, D., Guez-Haddad, J., Xue, W., Pan, W., et al. (2019). Leukocyte cytoskeleton polarization is initiated by plasma membrane curvature from cell attachment. Dev. Cell *49*, 206–219.e7. https://doi.org/10.1016/j.devcel.2019.02.023.
13. Schweitzer, Y., Lieber, A.D., Keren, K., and Kozlov, M.M. (2014). Theoretical analysis of membrane tension in moving cells. Biophys. J. *106*, 84–92. https://doi.org/10.1016/j.bpj.2013.11.009.
14. Tsai, T.Y.-C., Collins, S.R., Chan, C.K., Hadjitheodorou, A., Lam, P.-Y., Lou, S.S., Yang, H.W., Jorgensen, J., Ellett, F., Irimia, D., et al. (2019). Efficient front-rear coupling in neutrophil chemotaxis by dynamic myosin II localization. Dev. Cell *49*, 189–205.e6. https://doi.org/10.1016/j.devcel.2019.03.025.
15. Mueller, J., Szep, G., Nemethova, M., de Vries, I., Lieber, A.D., Winkler, C., Kruse, K., Small, J.V., Schmeiser, C., Keren, K., et al. (2017). Load adaptation of lamellipodial actin networks. Cell *171*, 188–200.e16. https://doi.org/10.1016/j.cell.2017.07.051.
16. Houk, A.R., Jilkine, A., Mejean, C.O., Boltyanskiy, R., Dufresne, E.R., Angenent, S.B., Altschuler, S.J., Wu, L.F., and Weiner, O.D. (2012). Membrane tension maintains cell polarity by confining signals to the leading edge during neutrophil migration. Cell *148*, 175–188. https://doi.org/10.1016/j.cell.2011.10.050.
17. Zmurchok, C., Collette, J., Rajagopal, V., and Holmes, W.R. (2020). Membrane tension can enhance adaptation to maintain polarity of migrating cells. Biophys. J. *119*, 1617–1629. https://doi.org/10.1016/j.bpj.2020.08.035.
18. Diz-Muñoz, A., Thurley, K., Chintamen, S., Altschuler, S.J., Wu, L.F., Fletcher, D.A., and Weiner, O.D. (2016). Membrane tension acts through PLD2 and mTORC2 to limit actin network assembly during neutrophil migration. PLoS Biol. *14*, e1002474. https://doi.org/10.1371/journal.pbio.1002474.
19. Neilson, M.P., Veltman, D.M., Haastert, P.J.M. van, Webb, S.D., Mackenzie, J.A., and Insall, R.H. (2011). Chemotaxis: a feedback-based

computational model robustly predicts multiple aspects of real cell behaviour. PLoS Biol. *9*, e1000618. https://doi.org/10.1371/journal.pbio.1000618.

20. Akamatsu, M., Vasan, R., Serwas, D., Ferrin, M.A., Rangamani, P., and Drubin, D.G. (2020). Principles of self-organization and load adaptation by the actin cytoskeleton during clathrin-mediated endocytosis. Elife *9*, e49840. https://doi.org/10.7554/eLife.49840.
21. Appadurai, D., Gay, L., Moharir, A., Lang, M.J., Duncan, M.C., Schmidt, O., Teis, D., Vu, T.N., Silva, M., Jorgensen, E.M., and Babst, M. (2020). Plasma membrane tension regulates eisosome structure and function. Mol. Biol. Cell *31*, 287–303. https://doi.org/10.1091/mbc.E19-04-0218.
22. Boulant, S., Kural, C., Zeeh, J.-C., Ubelmann, F., and Kirchhausen, T. (2011). Actin dynamics counteract membrane tension during clathrin-mediated endocytosis. Nat. Cell Biol. *13*, 1124–1131. https://doi.org/10.1038/ncb2307.
23. Gauthier, N.C., Fardin, M.A., Roca-Cusachs, P., and Sheetz, M.P. (2011). Temporary increase in plasma membrane tension coordinates the activation of exocytosis and contraction during cell spreading. Proc. Natl. Acad. Sci. USA *108*, 14467–14472. https://doi.org/10.1073/pnas.1105845108.
24. Riggi, M., Bourgoint, C., Macchione, M., Matile, S., Loewith, R., and Roux, A. (2019). TORC2 controls endocytosis through plasma membrane tension. J. Cell Biol. *218*, 2265–2276. https://doi.org/10.1083/jcb.201901096.
25. Thottacherry, J.J., Kosmalska, A.J., Kumar, A., Vishen, A.S., Elosegui-Artola, A., Pradhan, S., Sharma, S., Singh, P.P., Guadamillas, M.C., Chaudhary, N., et al. (2018). Mechanochemical feedback control of dynamin independent endocytosis modulates membrane tension in adherent cells. Nat. Commun. *9*, 4217. https://doi.org/10.1038/s41467-018-06738-5.
26. Basu, R., Whitlock, B.M., Husson, J., Le Floc'h, A., Jin, W., Oyler-Yaniv, A., Dotiwala, F., Giannone, G., Hivroz, C., Biais, N., et al. (2016). Cytotoxic T Cells Use Mechanical Force to Potentiate Target Cell Killing. Cell *165*, 100–110. https://doi.org/10.1016/j.cell.2016.01.021.
27. Masters, T.A., Pontes, B., Viasnoff, V., Li, Y., and Gauthier, N.C. (2013). Plasma membrane tension orchestrates membrane trafficking, cytoskeletal remodeling, and biochemical signaling during phagocytosis. Proc. Natl. Acad. Sci. USA *110*, 11875–11880. https://doi.org/10.1073/pnas.1301766110.
28. De Belly, H.D., Stubb, A., Yanagida, A., Labouesse, C., Jones, P.H., Paluch, E.K., and Chalut, K.J. (2021). Membrane tension gates ERK-mediated regulation of pluripotent cell fate. Cell Stem Cell *28*, 273–284.e6. https://doi.org/10.1016/j.stem.2020.10.018.
29. Bergert, M., Lembo, S., Sharma, S., Russo, L., Milovanović, D., Gretarsson, K.H., Börmel, M., Neveu, P.A., Hackett, J.A., Petsalaki, E., and Diz-Muñoz, A. (2021). Cell surface mechanics gate embryonic stem cell differentiation. Cell Stem Cell *28*, 209–216.e4. https://doi.org/10.1016/j.stem.2020.10.017.
30. Gudipaty, S.A., Lindblom, J., Loftus, P.D., Redd, M.J., Edes, K., Davey, C.F., Krishnegowda, V., and Rosenblatt, J. (2017). Mechanical stretch triggers rapid epithelial cell division through Piezo1. Nature *543*, 118–121. https://doi.org/10.1038/nature21407.
31. Horsnell, H.L., Tetley, R.J., De Belly, H., Makris, S., Millward, L.J., Benjamin, A.C., Heeringa, L.A., de Winde, C.M., Paluch, E.K., Mao, Y., and Acton, S.E. (2022). Lymph node homeostasis and adaptation to immune challenge resolved by fibroblast network mechanics. Nat. Immunol. *23*, 1169–1182. https://doi.org/10.1038/s41590-022-01272-5.
32. Li, J., Hou, B., Tumova, S., Muraki, K., Bruns, A., Ludlow, M.J., Sedo, A., Hyman, A.J., McKeown, L., Young, R.S., et al. (2014). Piezo1 integration of vascular architecture with physiological force. Nature *515*, 279–282. https://doi.org/10.1038/nature13701.
33. Yuge, S., Nishiyama, K., Arima, Y., Hanada, Y., Oguri-Nakamura, E., Hanada, S., Ishii, T., Wakayama, Y., Hasegawa, U., Tsujita, K., et al. (2022). Mechanical loading of intraluminal pressure mediates wound angiogenesis by regulating the TOCA family of F-BAR proteins. Nat. Commun. *13*, 2594. https://doi.org/10.1038/s41467-022-30197-8.
34. Shi, Z., Graber, Z.T., Baumgart, T., Stone, H.A., and Cohen, A.E. (2018). Cell membranes resist flow. Cell *175*, 1769–1779.e13. https://doi.org/10.1016/j.cell.2018.09.054.
35. Gomis Perez, C., Dudzinski, N.R., Rouches, M., Landajuela, A., Machta, B., Zenisek, D., and Karatekin, E. (2022). Rapid propagation of membrane tension at retinal bipolar neuron presynaptic terminals. Sci. Adv. *8*, eabl4411. https://doi.org/10.1126/sciadv.abl4411.
36. Ellefsen, K.L., Holt, J.R., Chang, A.C., Nourse, J.L., Arulmoli, J., Mekhdjian, A.H., Abuwarda, H., Tombola, F., Flanagan, L.A., Dunn, A.R., et al. (2019). Myosin-II mediated traction forces evoke localized Piezo1-dependent Ca2+ flickers. Commun. Biol. *2*, 298. https://doi.org/10.1038/s42003-019-0514-3.
37. Shi, Z., Innes-Gold, S., and Cohen, A.E. (2022). Membrane tension propagation couples axon growth and collateral branching. Sci. Adv. *8*, eabo1297. https://doi.org/10.1126/sciadv.abo1297.
38. Cohen, A.E., and Shi, Z. (2020). Do cell membranes flow like honey or jiggle like JellO? BioEssays *42*, e1900142. https://doi.org/10.1002/bies.201900142.
39. Saha, S., Town, J.P., and Weiner, O.D. (2023). mTORC2 coordinates the leading and trailing edge cytoskeletal programs during neutrophil migration. Mol. Biol. Cell *34*, ar35. https://doi.org/10.1091/mbc.E22-05-0191.
40. Town, J., and Weiner, O. (2023). Rac negative feedback links local PIP3 rate-of-change to dynamic control of neutrophil guidance. Preprint at bioRxiv. https://doi.org/10.1101/2022.12.30.521706.
41. Carlsson, A.E. (2018). Membrane bending by actin polymerization. Curr. Opin. Cell Biol. *50*, 1–7. https://doi.org/10.1016/j.ceb.2017.11.007.
42. Pontes, B., Viana, N.B., Salgado, L.T., Farina, M., Moura Neto, V.M., and Nussenzveig, H.M. (2011). Cell cytoskeleton and tether extraction. Biophys. J. *101*, 43–52. https://doi.org/10.1016/j.bpj.2011.05.044.
43. Pontes, B., Ayala, Y., Fonseca, A.C.C., Romão, L.F., Amaral, R.F., Salgado, L.T., Lima, F.R., Farina, M., Viana, N.B., Moura-Neto, V., and Nussenzveig, H.M. (2013). Membrane elastic properties and cell function. PLoS One *8*, e67708. https://doi.org/10.1371/journal.pone.0067708.
44. Roffay, C., Molinard, G., Kim, K., Urbanska, M., Andrade, V., Barbarasa, V., Nowak, P., Mercier, V., García-Calvo, J., Matile, S., et al. (2021). Passive coupling of membrane tension and cell volume during active response of cells to osmosis. Proc. Natl. Acad. Sci. USA *118*. e2103228118. https://doi.org/10.1073/pnas.2103228118.
45. Hoffstein, S.T., Friedman, R.S., and Weissmann, G. (1982). Degranulation, membrane addition, and shape change during chemotactic factor-induced aggregation of human neutrophils. J. Cell Biol. *95*, 234–241. https://doi.org/10.1083/jcb.95.1.234.
46. Evans, E., and Yeung, A. (1989). Apparent viscosity and cortical tension of blood granulocytes determined by micropipet aspiration. Biophys. J. *56*, 151–160.
47. Herant, M., Heinrich, V., and Dembo, M. (2005). Mechanics of neutrophil phagocytosis: behavior of the cortical tension. J. Cell Sci. *118*, 1789–1797. https://doi.org/10.1242/jcs.02275.
48. Ting-Beall, H.P., Needham, D., and Hochmuth, R.M. (1993). Volume and osmotic properties of human neutrophils. Blood *81*, 2774–2780.
49. Monge, G. (1781). Mémoire sur la Théorie des Déblais et des Remblais (De l'Imprimerie Royale).
50. Kantorovitch, L. (1958). On the translocation of masses. Manag. Sci. *5*, 1–4.
51. O'Neill, P.R., Castillo-Badillo, J.A., Meshik, X., Kalyanaraman, V., Melgarejo, K., and Gautam, N. (2018). Membrane flow drives an adhesion-independent amoeboid cell migration mode. Dev. Cell *46*, 9–22.e4. https://doi.org/10.1016/j.devcel.2018.05.029.
52. Borja da Rocha, H., Bleyer, J., and Turlier, H. (2022). A viscous active shell theory of the cell cortex. J. Mech. Phys. Solids *164*, 104876. https://doi.org/10.1016/j.jmps.2022.104876.

53. Turlier, H., Audoly, B., Prost, J., and Joanny, J.F. (2014). Furrow constriction in animal cell cytokinesis. Biophys. J. *106*, 114–123. https://doi.org/10.1016/j.bpj.2013.11.014.

54. Evans, E., and Rawicz, W. (1990). Entropy-driven tension and bending elasticity in condensed-fluid membranes. Phys. Rev. Lett. *64*, 2094–2097. https://doi.org/10.1103/PhysRevLett.64.2094.

55. Fournier, J.B., Ajdari, A., and Peliti, L. (2001). Effective-area elasticity and tension of micromanipulated membranes. Phys. Rev. Lett. *86*, 4970–4973. https://doi.org/10.1103/PhysRevLett.86.4970.

56. Raucher, D., and Sheetz, M.P. (1999). Characteristics of a membrane reservoir buffering membrane tension. Biophys. J. *77*, 1992–2002. https://doi.org/10.1016/S0006-3495(99)77040-2.

57. Svitkina, T.M. (2020). Actin cell cortex: structure and molecular organization. Trends Cell Biol. *30*, 556–565. https://doi.org/10.1016/j.tcb.2020.03.005.

58. Bisaria, A., Hayer, A., Garbett, D., Cohen, D., and Meyer, T. (2020). Membrane proximal F-actin restricts local membrane protrusions and directs cell migration. Science *368*, 1205–1210. https://doi.org/10.1126/science.aay7794.

59. Welf, E.S., Miles, C.E., Huh, J., Sapoznik, E., Chi, J., Driscoll, M.K., Isogai, T., Noh, J., Weems, A.D., Pohlkamp, T., et al. (2020). Actin-membrane release initiates cell protrusions. Dev. Cell *55*, 723–736.e8. https://doi.org/10.1016/j.devcel.2020.11.024.

60. Diz-Muñoz, A., Fletcher, D.A., and Weiner, O.D. (2013). Use the force: membrane tension as an organizer of cell shape and motility. Trends Cell Biol. *23*, 47–53. https://doi.org/10.1016/j.tcb.2012.09.006.

61. Bornschlögl, T., and Bassereau, P. (2013). The sense is in the fingertips: the distal end controls filopodial mechanics and dynamics in response to external stimuli. Commun. Integr. Biol. *6*, e27341. https://doi.org/10.4161/cib.27341.

62. Bornschlögl, T., Romero, S., Vestergaard, C.L., Joanny, J.F., Van Nhieu, G.T., and Bassereau, P. (2013). Filopodial retraction force is generated by cortical actin dynamics and controlled by reversible tethering at the tip. Proc. Natl. Acad. Sci. USA *110*, 18928–18933. https://doi.org/10.1073/pnas.1316572110.

63. Schindelin, J., Arganda-Carreras, I., Frise, E., Kaynig, V., Longair, M., Pietzsch, T., Preibisch, S., Rueden, C., Saalfeld, S., Schmid, B., et al. (2012). Fiji: an open-source platform for biological-image analysis. Nat. Methods *9*, 676–682. https://doi.org/10.1038/nmeth.2019.

64. Sofroniew, N., Lambert, T., Evans, K., Nunez-Iglesias, J., Bokota, G., Winston, P., Peña-Castellanos, G., Yamauchi, K., Bussonnier, M., Doncila Pop, D., et al. (2022). Napari: a multi-dimensional image viewer for Python. Zenodo. https://doi.org/10.5281/zenodo.7098045.

65. Fonseca, J.P., Bonny, A.R., Kumar, G.R., Ng, A.H., Town, J., Wu, Q.C., Aslankoohi, E., Chen, S.Y., Dods, G., Harrigan, P., et al. (2019). A toolkit for rapid modular construction of biological circuits in mammalian cells. ACS Synth. Biol. *8*, 2593–2606. https://doi.org/10.1021/acssynbio.9b00322.

66. van der Walt, S., Schönberger, J.L., Nunez-Iglesias, J., Boulogne, F., Warner, J.D., Yager, N., Gouillart, E., and Yu, T.; scikit-image Contributors (2014). scikit-image: image processing in Python. PeerJ *2*, e453. https://doi.org/10.7717/peerj.453.

67. Virtanen, P., Gommers, R., Oliphant, T.E., Haberland, M., Reddy, T., Cournapeau, D., Burovski, E., Peterson, P., Weckesser, W., Bright, J., et al. (2020). SciPy 1.0: fundamental algorithms for scientific computing in Python. Nat. Methods *17*, 261–272. https://doi.org/10.1038/s41592-019-0686-2.

STAR★METHODS

KEY RESOURCES TABLE

REAGENT or RESOURCE	SOURCE	IDENTIFIER
Chemicals, peptides, and recombinant proteins		
RPMI 1640 supplemented with L-glutamine and 25 mM HEPES	Corning	10-041-CM
Bovine Serum Albumin (endotoxin-free, fatty acid free)	Sigma-Aldrich	A8806
Heat-inactivated fetal bovine serum	Gibco	16140071
DMEM	Corning	10-017-CV
Bovine Calf Serum	Sigma-Aldrich	12138C
Latrunculin B	Sigma-Aldrich	76343-94-7
NSC668394	Sigma-Aldrich	341216
Carboxyl latex bead	Invitrogen	C37278
Concanavalin A	Sigma-Aldrich	C2272
SPY650-FastAct™	Cytoskeleton	CY-SC505
CellMask™ Deep Red	Thermofisher	C10046
Janelia Fluor 646	Janelia	JF646X
Lenti-X Concentrator	Clontech	631231
TransIT-293 Transfection Reagent	Mirus Bio	MIR2705
96-well #1.5 glass-bottom plates	Azenta Life Sciences	4ti-0223
u-Flux™ flow cell (70-mm chips)	Lumicks	C1
Glass capillary tube	King Precision Glass	KG-33
Deposited data		
Optimal transport and model	GitHub Zenodo	Github: https://github.com/VirtualEmbryo/membrane-cortex-tension; Zenodo: https://doi.org/10.5281/zenodo.7894202
Bleaching & gaussian fitting	GitHub Zenodo	Github: https://github.com/weinerlab/Inverse_Photobleach_Flow; Zenodo: https://doi.org/10.5281/zenodo.7894212
Experimental models: Cell lines		
HL-60s	Bourne lab	N/A
Opto-PI3K HL-60s	Weiner lab	N/A
Opto-LARG HL-60s	Weiner lab	N/A
3T3-Swiss Albino	UCSF cell culture facility	CCLZR083
HEK293T	UCSF cell culture facility	CCLZR076
Software and algorithms		
Fiji	Schindelin et al[63]	N/A
Prism 9	Graphpad software, Inc	N/A
Adobe Illustrator	Adobe	N/A
Excel	Microsoft	N/A
Napari	Sofroniew et al[64]	N/A

RESOURCE AVAILABILITY

Lead contact

Further information and requests for resources and reagents should be directed to and will be fulfilled by the lead contact, Orion Weiner (orion.weiner@ucsf.edu)

Materials availability

All unique/stable reagents generated in this study are available from the lead contact without restriction.

Data and code availability

- All data reported in this paper will be shared by the lead contact upon request.
- All original code has been deposited on GitHub and Zenodo and is publicly available as of the date of publication.
- Any additional information required to reanalyze the data reported in this paper is available from the lead contact upon request.

EXPERIMENTAL MODEL AND SUBJECT DETAILS

HL-60 cells are from the laboratory of Henry Bourne and were recently verified via STR profiling in.[39] HL-60s were cultured in R10 growth medium, which is RPMI 1640 supplemented with L-glutamine and 25 mM HEPES (Corning; Corning, NY) and containing 10% (v/v) heat-inactivated fetal bovine serum (Gibco; Waltham, MA). Cultures were kept at a density of 0.2–1.0 million cells/mL at 37°C/5% CO_2.

HEK293T cells (used to make lentivirus for transduction of HL-60s) are from UCSF cell culture facility (CCLZR076) and were grown in DMEM (Corning; Corning, NY) containing 10% (v/v) heat-inactivated fetal bovine serum (Gibco; Waltham, MA) and maintained at 37°C/5% CO_2. All media were 0.22-um filtered.

Opto-PI3K cells (iLid-BFP-CAAX, iSH2-GFP, Pak-PBD-mCherry) were obtained from.[39] Plasmids used to generate Opto-LARG cells (iLid-BFP-CAAX, DHPH-ARHGEF1-GFP, AnillinRBD-mCherry), Opto-PI3K expressing CAAX-HaloTag, and Actin-HaloTag were assembled using a Golden-Gate-based modular cloning toolkit.[65].

3T3-Swiss Albino were obtained from UCSF cell culture facility (CCLZR083) and were cultured in DMEM (Corning; Corning, NY) supplemented with 10% Bovine Calf Serum (Sigma; St. Louis, MO, 12138C) and maintained at 37°C/5% CO_2

METHOD DETAILS

Transduction of HL-60 cells

HEK293T cells were used to generate lentivirus and were seeded into 6-well plates until approximately 80% confluent. For each transduction, 1.5 μg pHR vector (containing the appropriate transgene), 0.167 μg vesicular stomatitis virus-G vector, and 1.2 μg cytomegalovirus 8.91 vector were prepared for transfection using TransIT-293 Transfection Reagent (Mirus Bio; Madison, WI). Three days post transduction virus-containing supernatants were harvested and concentrated approximately 40-fold using Lenti-X Concentrator (Clontech; Mountainview, CA). Concentrated viruses were frozen and stored at −80°C until needed. For all transductions, thawed virus was mixed with approximately 0.3 million cells in growth media supplemented with polybrene (8 μg/mL) and incubated overnight. Cells expressing desired transgenes were isolated using fluorescence-activated cell sorting (FACS) as appropriate (FACSAria2; BD Biosciences; Franklin Lakes, NJ).

Microscopy hardware

Imaging depicted in Figures 1B; 4A, 5B, S4A, S4D, S4F, S5E, S5I, and S6N and Videos S1, S3, and S4 were performed at 37°C on a Nikon Eclipse Ti inverted microscope equipped with a Borealis beam conditioning unit (Andor), a CSU-W1 Yokogawa spinning disk (Andor; Belfast, Northern Ireland), a 100X PlanApo TIRF 1.49 numerical aperture (NA) objective (Nikon; Toyko, Japan), an iXon Ultra EMCCD camera (Andor), and a laser merge module (LMM5, Spectral Applied Research; Exton, PA) equipped with 405, 440, 488, and 561-nm laser lines. All hardware was controlled using Micro-Manager (UCSF).

Optogenetic activation was performed using a LED (470-nm) via a custom DMD (Andor Technology). Illumination intensities were varied by connecting the LEDs to the analog outputs of a digital-to-analogue converter and setting the LED voltages using serial commands via custom Python code. The microscope is equipped with two stacked dichroic turrets such that samples can be simultaneously illuminated with LEDs and imaged using a 488-nm long-pass dichroic filter (Chroma Technology Corp.)

Preparation of Opto-PI3K and Opto-LARG cells for confocal imaging

For experiments in which we monitored cells by confocal imaging, cells were seeded in a 96-well #1.5 glass-bottom plates (Azenta Life Sciences) in R+B imaging media, which is RPMI 1640 supplemented with L-glutamine and 25 mM HEPES (Corning; Corning, NY) and containing 0.2% Bovine Serum Albumin (BSA, endotoxin-free, fatty acid free; A8806, Sigma; St. Louis, MO). For optogenetic activation, cells were illuminated using DMD (see above) at a chosen location (using custom Python code) in a circular pattern of varying size (∼2 microns radius for Opto-PIK, ∼1 micron radius for Opto-LARG) for a duration of 90 seconds. For Figures S6M–S6P, we imaged the cells using a two-step Z-stack of the ventral side (∼TIRF plane) and mid-section of the cell.

For plasma membrane and actin imaging using HaloTag (Figures 1B, 4A, S4F, S4M, S4P, S4Q, and S6N), cells were stained with 100nM of JF646X for 10 min before being pelleted at 300*g* for 3 min and resuspended in R+B imaging media (RPMI+0.2% BSA).

For plasma membrane imaging using the membrane dye CellMask (Figures 5B, 5I, and S4D), cells were first incubated with ~2-5μg/ml of CellMask™ Deep Red (C10046, Thermofisher) for 3 minutes at 37°C/5% CO_2. Cells were then pelleted at 300*g* for 3 min and resuspended in R+B imaging media (RPMI+0.2% BSA).

For actin imaging of Opto-LARG (Figures S5E and S5I), cells were incubated with the actin dye SPY650-FastAct™ (CY-SC505) for 1h at 37 C/5% CO_2. Cells were then pelleted at 300*g* for 3 min and resuspended in R+B imaging media (RPMI+0.2% BSA).

Preparation, settings, and operation procedures for membrane tethering pulling experiments on C-trap® optical tweezers with confocal imaging

Cell preparation

Opto-PI3K & Opto-LARG: 1-1.5 ml cells (from culture at density of 0.6–0.8 million cells/mL) were stained (with 0.5 μl of CellMask™ Deep Red or 100nM of JF646X), then pelleted down and resuspended in either R+B imaging medium (RPMI+0.2% BSA) or R10 medium (all media 0.22-um filtered) in the absence or presence of actin inhibitor (10 μM Latrunculin B) for samples used in tether pulling assay.

To heavily depolymerize the cortex (Figures 3G–3K and S3G–S3J) Cells were resuspended in a hypotonic media 60% H2O and 40% R10) containing 10 μM Latrunculin B.

To decreases membrane-to-cortex attachment (Figures 6D–6G and S6C), cells were resuspended in media (R10) containing 25μM of Ezrin inhibitor NSC668394 (Sigma-Aldrich, 341216).

Bead preparation

In a 1.7 ml Eppendorf tube, the following solutions were added: 9 μl of ultrapure water (Corning, 46-000-CM), 9 μl of carboxyl latex bead (4% w/v, 2 μm; Invitrogen, C37278), and 2 μl of Concanavalin A (1 mg/ml; Sigma-Aldrich, C2272); sample was vortexed at low speed at room temperature for 45-60 min; 1-2 μl of this bead mixture stock was added into 1 ml of RPMI 1640 buffer (0.22-um filtered) for samples used in tether pulling assay.

Microfluidics

An u-Flux™ flow cell (70-mm chips; Lumicks, C1), installed on an heat-insulating PVC holder, was passivated with R+B imaging media (0.22-um filtered) and pre-warmed at 35-37°C for 1-2 hours. A custom-made microchamber integrated with micropipettes (descriptions on the assembly provided at the end) was used in place of u-Flux™ flow cell to apply aspiration in tether pulling assay performed on C-trap® (instrument operation procedures in the next section). During the assay, an air-pressured microfluidics flow system (u-Flux™, Lumicks), with pre-cleaned and proper dimensions of tubing connections, was used to deliver cell samples, bead solutions, and blank media/buffers (for flushing) into the flow cell or microchamber. Specifically, a tubing with large ID (1/32 inch; Idex, 1520L) was used to deliver cells at the lowest pressure setting (0.04-0.12 mbar, or sometimes just gravity flow) so as to minimize the shear force exerted to the cells during delivery. The delivery of beads and media was made with a narrower tubing (ID 0.004 inch; Upchurch Scientific, PM-1148-F). After flowing ~200-500 μl (sufficient to displace dead volumes combined within the microfluidics system) of cells into the C-trap® system pre-warmed at ~36°C, incubated for 15-20 min so that the cells settle and stably attach to the bottom surface of the u-Flux™ flow cell. Cell locations were then marked prior to the subsequent tether pulling experiments with optical traps. The cell samples were replenished every 1.5-2 hours, with abundant flushing of R+B imaging medium in between (which ensures the flow cell surface remains properly passivated).

Optical trapping – setting and operations

A commercial dual-trap optical tweezers with 3-color confocal imaging, aka C-trap®, from Lumicks was used to perform the tether pulling assay with concurrent fluorescence imaging. The flow cell, or microchamber, held paralleled to the table surface was aligned perpendicular between a water objective (60x, NA 1.2; Nikon, MRD07602) coming from the bottom and a matching condenser (60x, NA 1.4, used with Type A immersion oil; Leica) coming from the top. The flow cell was positioned in between the two such the IR laser beams (1064 nm) focused down by the objective were formed inside the flow cell ~10-20 μm above the inner bottom surface (with the flow cell nano-stage set at the middle position). After the flow cell, the condenser can adequately collect photons from the IR trapping beams and project on to position-sensitive detectors (PSDs) for accurate trap force measurement (data acquisition at a rate of 78125 Hz and later down sampled to 10 Hz for analysis). The objective also directs fluorescence excitations in the visible wavelength range (488, 532, and 642 nm respectively for opto-tool, Rac/RhoA biosensor, and CellMask/HaloTag) into the flow cell (or microchamber). The two set of light sources (IR and visible) were controlled by separate telescopes and mirror-steering systems upstream from the objective. The same objective collected the emission photons from the imaging/optical trapping sample plane inside the flow cell for fluorescence imaging (bandpass filters: 512/25, 582/75, and 680/42; camera pixel size: 100 nm; frame rate depends on confocal scanning area size), whereas the condenser provided bright field imaging (850 nm LED light source) recorded at 10 Hz.

Both the objective and the condenser were pre-warmed to 35-37°C (temperature control unit, Lumicks) for at least 2-3 hours prior to cell experiments. The IR trapping power was typically set at 100% trapping laser, 10% overall power, and 50-50 split between trap 1 (T1) and trap 2 (T2), which is about ~175 mW per trap (measured at the objective front) and ~0.2 pN/nm in trap stiffness for a 2-μm bead (bead corner frequency ~2500 Hz). Low settings of excitation laser were sufficient for fluorescence imaging (typically ~2-5% of total power gives ~0.02-0.04 μW measured at the objective front), minimizing the photo-toxicity to the cell during experiments.

At the beginning of each cell recording in the tether pulling assay, 2-μm Concanavalin-coated beads were flowed into the microchamber (e.g., at 0.4 mbar via channel 5 in u-Flux™ C1 flow cell) and single beads were captured in either one or both traps; we then moved the flow cell stage to bring the beads to a cell location marked after incubation (as described earlier). With beads in the vicinity of the cell, i.e., in z-axis at the same confocal imaging plane for the cell (∼2-6 μm from the flow cell bottom surface) and ∼4-6 μm away from the cell body in the x-y plane, the trap stiffness was calibrated, and any residual force readout were zeroed before engaging the bead with the cell body to form membrane tethers. Region of interest (ROI) was cropped for bright field imaging (typically an area of 35x45 μm), and continuous recording at 10 Hz was initiated.

1. Tether pulling assay with light-activated cell protrusions: as seen from the bright field camera, we approached beads to position them in direct contact with the cell body (even pressing a little, judging from the counter force acted on the bead in the trap), then we waited for several seconds before carefully (slowly) pulling out membrane tethers (∼4-10 μm in length) at the desired con Figuration (e.g., two tethers right angle from each other). We monitored steady state tension for at least 1 min (Figure S1G) before local 488-nm excitation (ROI: 6x10 μm) continuously for 90 sec on the opposite site of (or right angle from) the membrane tether. Upon localized 488-nm illumination, the local recruitment of opto-controls (iSH2 labelled with EGFP) to trigger cell protrusions was also imaged simultaneously (∼1-1.3 sec/frame scanned). Post protrusion activation, we monitored cell membrane tension recovery for 180 sec and repeated activation cycles for as long as the tethers last (see Video S2). At desired time points, i.e., before, during, or after 488-nm light activation, the activated Rac was specifically imaged via 532-nm illumination to visualize the distribution of the Rac biosensor (Pak-PDB-mCherry) inside the cell (see Figures S1B–S1E and Video S1). Similarly, the changes in cell membrane morphology were imaged over time with 642-nm illumination (for CellMask Deep Red or Halo-tag 660 if cells were stained earlier).
2. Other experimental conditions in tether pulling assay, including controls: following the same bead engagement procedure described above, membrane tethers were pulled out from the cell body or from small patches of vesicle-like, outward budding membrane blebs that are detached from actin cortex upon Latrunculin treatment. Specifically, after the first membrane tether was formed, the second tether was pulled from a nearby location ∼2 μm away. The membrane tension was recorded in the same fashion as detailed earlier but for the following conditions: light activation on wild-type cells or drug-treated opto-PI3K cells; in the absence of any light illumination, we moved one trap to extend the length of one tether on the cell body (or bleb) and monitor the tension response on the other (see Video S2); or instead of 488-nm illumination (which triggers actin-driven cell protrusion), the cell was engaged with micropipette aspiration, which exerts mechanical pulling on both membrane and cortex, and the membrane tension was recorded over cycles of aspiration and relaxation (see below; Video S5). For Figures S6A–S6B, we pulled tethers from either HL-60s or 3T3 cells at a constant rate until eventual tether breakage (following method from Raucher and Sheetz[56]). We then measured the bead-to-cell distance at the point of tether rupture as detected by our force measurements.

At the end of each measurement, unless tethers had already broken on their own or by debris falling into the trap, trapping lasers were turned off to observe the tether and bead elastic recoil toward the cell as a control of the absence of cytoskeleton in the tethers (Figures 1D, S3C, and S3J and Video S1).

Micropipette aspiration

A custom-made microchamber was used to implement micropipette aspiration on the C-trap® system. Specifically, a micropipette of 2-6 um tip diameter was prepared by gravity pulling a thin glass capillary tube (ID 0.040 +/- 0.010 mm, OD 0.080 +/- 0.010 mm, length 150 mm; King Precision Glass, KG-33) that was threaded through a heated platinum coil (∼2 mm in diam.; Pt wire is 0.3 mm in diam., Alfa Aesar) upon application of a desired voltage. The micropipette tip size generally correlates with the heating time required to pull the glass tube apart; the faster heating, the more rapid the pull, giving micropipette tips in smaller diameters. The micropipette was then sandwiched between a 1-mm glass cover slide (3''x1''x 1 mm; VWR) and a #1.5 glass cover slip (24x60 mm; VWR), held together with two pieces of melted Nescofilm (100 um in thickness; Karlan) as sealant and spacer in the microchamber. 6 holes were drilled prior on the glass slide to provide inlets, which are connected to valves and uFlex™ pressurized syringe reservoirs (for cell and bead samples delivery as well as buffer flushing), and outlets towards the waste collection. The micropipette was connected to a separated microfluidic pressurized system (MFCS™-EZ from Fluigent; input: -600 mbar, output: -69 to 0 mbar) powered by a small floor pump (KNF, model: N86KN.18, with manual regulator) to provide aspiration control in the tether pulling assay on C-trap®. The aspiration pressure zero point for each micropipette was carefully calibrated and set to have no outward nor inward flow detectable to a laser trapped bead that was placed at the tip opening of the micropipette. During the experiments, cells were delivered into the microchamber at the same gentle flow rate (0.04-0.12 mbar, or sometimes just gravity flow) and captured by the optical trap, which quickly brings the cell to the micropipette tip. A minute amount of suction was applied to keep the cell stably engage with the tip (so it neither floats away from the tip nor falls back into the optical trap) but without any visible deformation of the cell morphology (as seen in bright field camera). Then following the same bead calibration procedure and membrane tether pulling process as described earlier, consecutive rounds of aspiration and relaxation were performed on the cell for as long as the membrane tethers persist (see Video S5).

QUANTIFICATION AND STATISTICAL ANALYSIS

Image and membrane tension analysis

Fiji (NIH),[63] Excel (Microsoft; Redmond, WA), custom Python code, and Prism (Graphpad software, Inc) were used for image and membrane tension analysis. Average trap force plots (Figures 1F, 2E, 5D, 5G, 6E, 6G, S1J, S2A–S2B, and S5C) were obtained by aligning trap force traces at time of light induction.

Average linked trap force plots were made using Prism Graphpad (software, Inc). In Figures 1G and 5E, average trace trap force was measured for 60 seconds before light induction (steady state) and for the duration of the light induction (90 seconds, Light). For Figure 6J, average trace trap force shown here for 30 seconds before aspiration (steady state), for the duration of aspiration (15-30 seconds), and for intervening recovery periods.

Pearson correlation coefficients between T1 and T2 were calculated using Prism Graphpad software, Inc) (Figures 2F, 3J, 5H, and S6K). For Figures 2F and 3J, we used 30 seconds before activation for steady state, 30 seconds of light induction for opto-activated protrusion, and ~10-30 seconds of active tether pulling on cell membrane (tether length >30 μm) and on blebs. In Figure 2F, for '+Light' we used the full duration of light activation (90sec) and for 'Recovery' 70sec post light induction. In Figure S6K we used 15-30 sec pre-aspiration for steady state value and full duration of aspiration (~15-30sec) for aspiration.

Delay between T2 and T1 during light induced protrusion (Figures 2D, S5D, and S6J) was calculated by measuring the time difference between light induction and change in trap force slope for each trap. Of note, measuring time difference from light induction to plateau in force increase yields similar results (i.e., delay time between the two traps is still of ~ 1 sec).

For measurement of relative tether force over distance of moving tether (Figure 3K), we normalized the trap force of static tether by its average when the extending tether was at distance <1 μm (namely, before any active pulling).

For Figures S5E–S5F, we observed that FastAct (see above) intensity linearly increases during imaging. To make sure that these increases did not interfere with our quantifications, we used a set of ~40 unstimulated cells, acquired in parallel of every Opto-LARG experiments using FastAct and corrected our measured fluorescence intensity to compensate for this passive intensity increase.

For Figure S1F, in combination to trap forces measurements (see above), cell diameter at the long axis was measured using a custom Fiji plugin and brightfield imaging from optical trap setup as a proxy to roughly approximate cell shape changes during light-induced protrusions.

For Figure S4Q, microvilli tracking was achieved by manually tracking microvilli over consecutive time frames using HaloTag-CAAX (see above) as membrane marker.

For Figure S5I, Actin speckle tracking was achieved by using actin dye FastAct (see above) and by manually tracking distinct actin features (e.g., high intensity points) over consecutive time frames.

For tether length tracking (Figures 1D, 3B, 3E, 3H, 3K, S3A–S3C, S3I, and S3J), we used a custom-made Fiji macro tracking the position of the bead overtime using brightfield recordings during optical trapping experiments. The timestamps for turning the trap off were also recorded.

In Figure 4G, kymographs were generated by segmenting the cell body through the HT-CAAX (JFX-549) channel and finding the three-pixel wide boundary pixels that best capture the membrane of the CellMask channel. This segmented cell outline is unraveled and averaged over every three values to provide 1 x N arrays which are stacked to show the evolution of membrane signal over time. Image segmentation code utilized the Python package Scikit-Image.[66]

In Figure 4H,

$$f(x) = m \cdot e^{\left(-\frac{(x-c)^2}{2r_0^2}\right)} + o$$

CellMask signal along the membrane is fitted with the parametric extension of the gaussian equation defined as:

where x is the distance along the cell's perimeter in μm, m is the peak of the CellMask signal, r0 is the width of the CellMask signal, c position of the peak CellMask signal, and o is the offset of the CellMask signal from zero. The shift in the peak CellMask signal along the membrane was quantified over time for both control and protruding cells in Figure 4I. Membrane flow rates were calculated by taking the slope of the fitted linear regression lines and averaging the flow rates within the control and protruding groups. Code for gaussian and linear regression fitting utilized the curve_fit and linregress functions in the Python package Scipy.[67] Image analysis and gaussian fitting code in available on Github and Zenodo.

Statistical analysis

For all statistical analysis, PRISM 9 (Graphpad software, Inc) was used. Statistical details can be found in the legend of each figure. N represents number of independent biological replicates. Pooled independent experiments are used in dot plots. Unless specified otherwise, error bars always represent SD.

CellPress
OPEN ACCESS

Supplemental figures

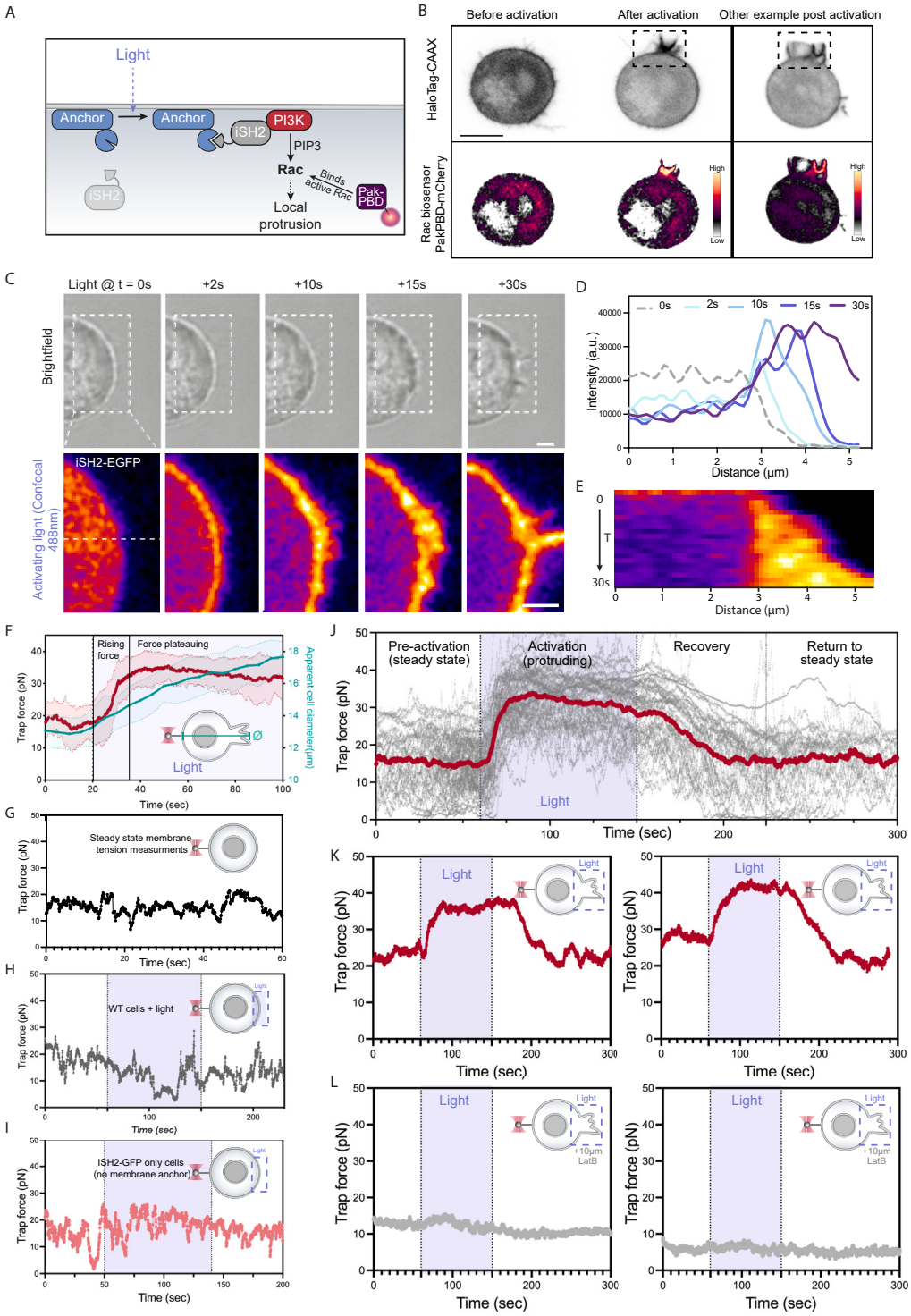

(legend on next page)

Figure S1. Optogenetic control of PI3K leads to local Rac activation, which triggers localized actin-driven cell protrusion and rapid membrane tension increase, related to Figure 1

(A) Membrane-anchored optogenetic control for light-induced activation of phosphoinositide 3-kinase (PI3K): upon localized 488-nm excitation, the membrane anchor protein (iLid-BFP-CAAX) undergoes a conformational change, which results in the binding of inter SH2 domain (iSH2) to the illuminated region. iSH2 proceeds to recruit PI3K, whose lipid product (PIP_3) induces the activation of Rac GTPase (Rac). Active Rac then triggers actin polymerization leading to localized membrane protrusion. By imaging the mCherry-labeled Rac biosensor (Pak-PBD-mCherry), which recognizes and binds the active GTP-bound Rac, we can monitor Rac activation during light-induced protrusions (see STAR Methods).

(B) Time-lapse confocal images of HL-60 cells expressing opto-construct (Opto-PI3K), membrane marker (CAAX-HaloTag, imaged on top), and Rac biosensor (PAK-PBD-mCherry, imaged on bottom). Middle and right: localized recruitments of active Rac is confirmed at the site of light activation for cell protrusion (box in black dashed line). Scale bar: 5 μm.

(C) Time-lapse brightfield (top) and confocal images (bottom) of an opto-PI3K cell during light activation. The specific recruitment of PI3K activator, (iSH2-EGFP) to the illuminated area (box in white dashed line) is monitored upon 488-nm excitation. Within 2 s (between the first two frames), iSH2 has redistributed from the cytoplasm to the plasma membrane. Scale bar: 1 μm.

(D) Fluorescence intensity line scans (along the white dashed line in (C) show the enrichment of opto-construct (iSH2-GFP) at the cell protruding site over time.

(E) Kymograph of the above line scan (white dashed line in C) shows that after iSH2 is recruited to the membrane, the cell contour (i.e., its membrane) rapidly expands outward.

(F) In red, average time trace of cells before and during light-induced protrusion. In green, apparent cell diameter (long axis) over time as proxy of cell shape change and increases in apparent surface area during protrusion. Trap force and shape change are correlated during the initial phase of the protrusion (rising phase) but then are decoupled as the cell access its membrane reservoirs limiting further increases in membrane tension (plateau phase) even as the protrusion continues to extend (means ± SD; n = 15, N = 5).

(G) Representative time trace of trap force measured from the tether pulling assay with a cell at steady state: membrane tension remains stable with low magnitude of stochastic fluctuations.

(H) As a control, we light activate the wild-type (WT) cells, which lack opto-constructs, and use the same tether pulling assay described above to monitor membrane tension response before, during, and after 488-nm illumination (purple shaded area). Representative time trace of trap force for cell membrane tension recorded from WT cells with light activation. The activation light alone does not elicit any changes in cell morphology or membrane tension responses.

(I) In another control, we light activate cells lacking the membrane anchor protein for opto-control (iLid-BFP-CAAX) and monitor their membrane tension response upon 488-nm illumination (purple shaded area). No perceptible changes in cell morphology or membrane tension were observed.

(J) Averaged time trace of trap force (red) for cell membrane tension recorded before (steady state), during (activation), and after (recovery and return to steady state) light-induced protrusion on the opposite side of the cell (see Figure 1C). Individual data traces are shown in light gray (same data as in Figure 1F, n > 60, N = 8). Cells at steady state exhibit stochastic fluctuations in membrane tension, similar to that shown earlier in (G). Upon light activation (purple shaded area), membrane tension rapidly increases and levels off to a plateau toward the end of activation (total 90 s). The presence of a plateau potentially indicates that membrane reservoirs unfold to provide extra membrane, thus buffering the tension rise. Shortly after the activation light is turned off, membrane tension gradually decreases to the steady-state level.

(K) Two example time traces of trap force for membrane tension before, during, and after light-induced cell protrusion.

(L) Same as (K) but recorded from cells treated with actin inhibitor (10 μM latrunculin B). We verified that latrunculin B treatment neither impairs the opto-tool recruitment nor the subsequent Rac activation. This control shows that the increase in membrane tension measured at the opposite side of cell protrusion is dependent on the actin cytoskeleton.

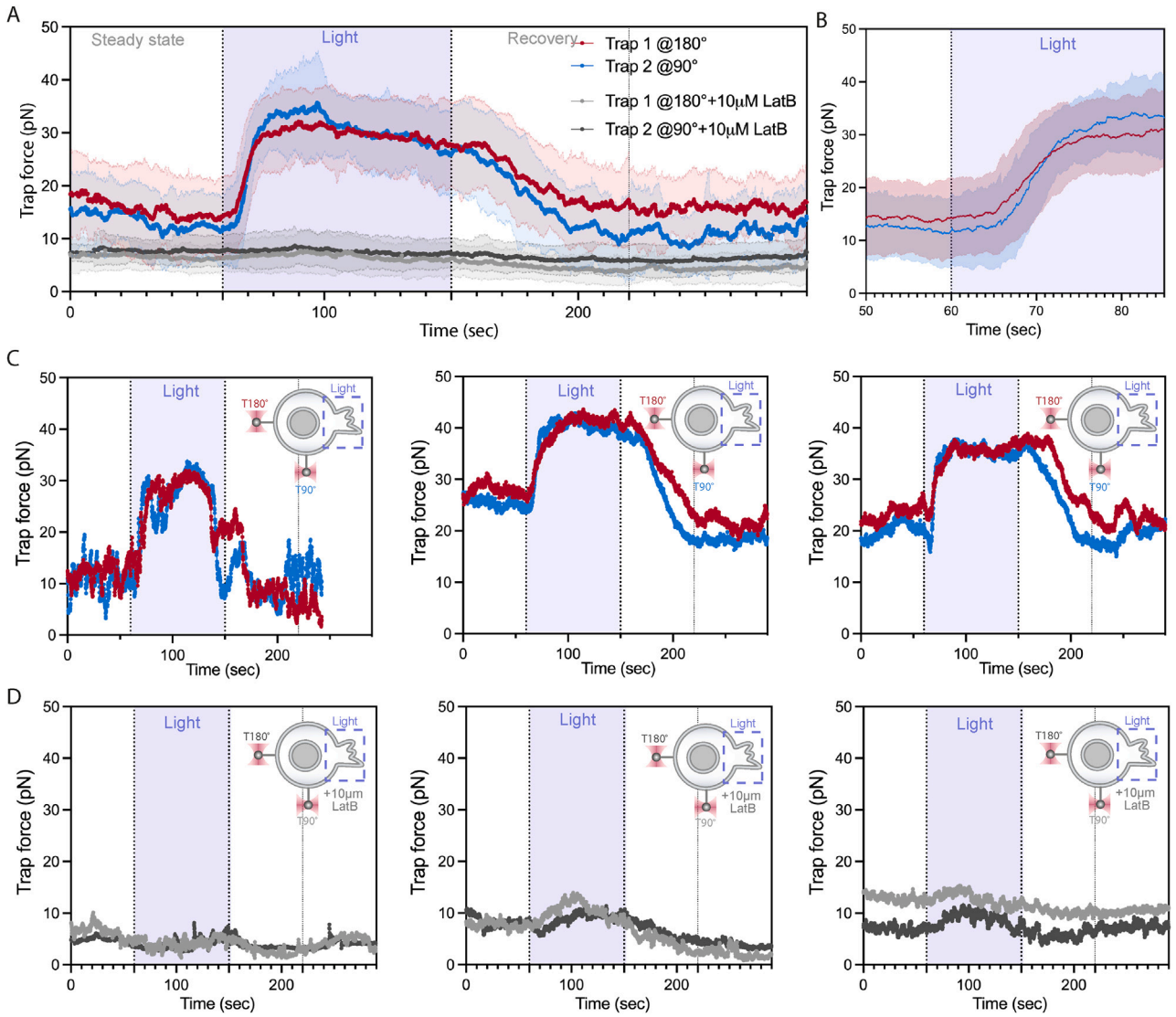

Figure S2. Membrane tension propagates within seconds across the cell during actin-driven protrusion, related to Figure 2

(A) Red and blue: averaged time traces of trap force for dual membrane tension measurements before (steady state), during (light), and after (recovery) activating cell protrusion. A nearly coinciding tension increase is observed between the membrane tether adjacent to (trap 2, blue) and opposite from (trap 1, red) cell protrusion. Gray: as a control, averaged trace from cells treated with actin inhibitor (10 μM latrunculin B) shows no membrane tension change upon activation (means ± SD; n > 15, N > 4).

(B) Zoom-in on traces in (A): increases in membrane tension emerge on both tethers within the first 5–10 s of light activation.

(C) Three example time traces of trap force for dual membrane tension measurements before, during, and after light-induced cell protrusion. At steady state, tensions from the two tethers show little correlation, but they become highly correlated upon light activation (purple shaded area). During the recovery phase, we often observe a lag in time between the two tethers' tension drop, with the tether opposite from the protrusion site recovering more slowly (red).

(D) Three example time traces of trap force for dual membrane tension measurements with cells treated with actin inhibitor (10 μM latrunculin B) before, during (purple shaded area), and after light activation of cell protrusion.

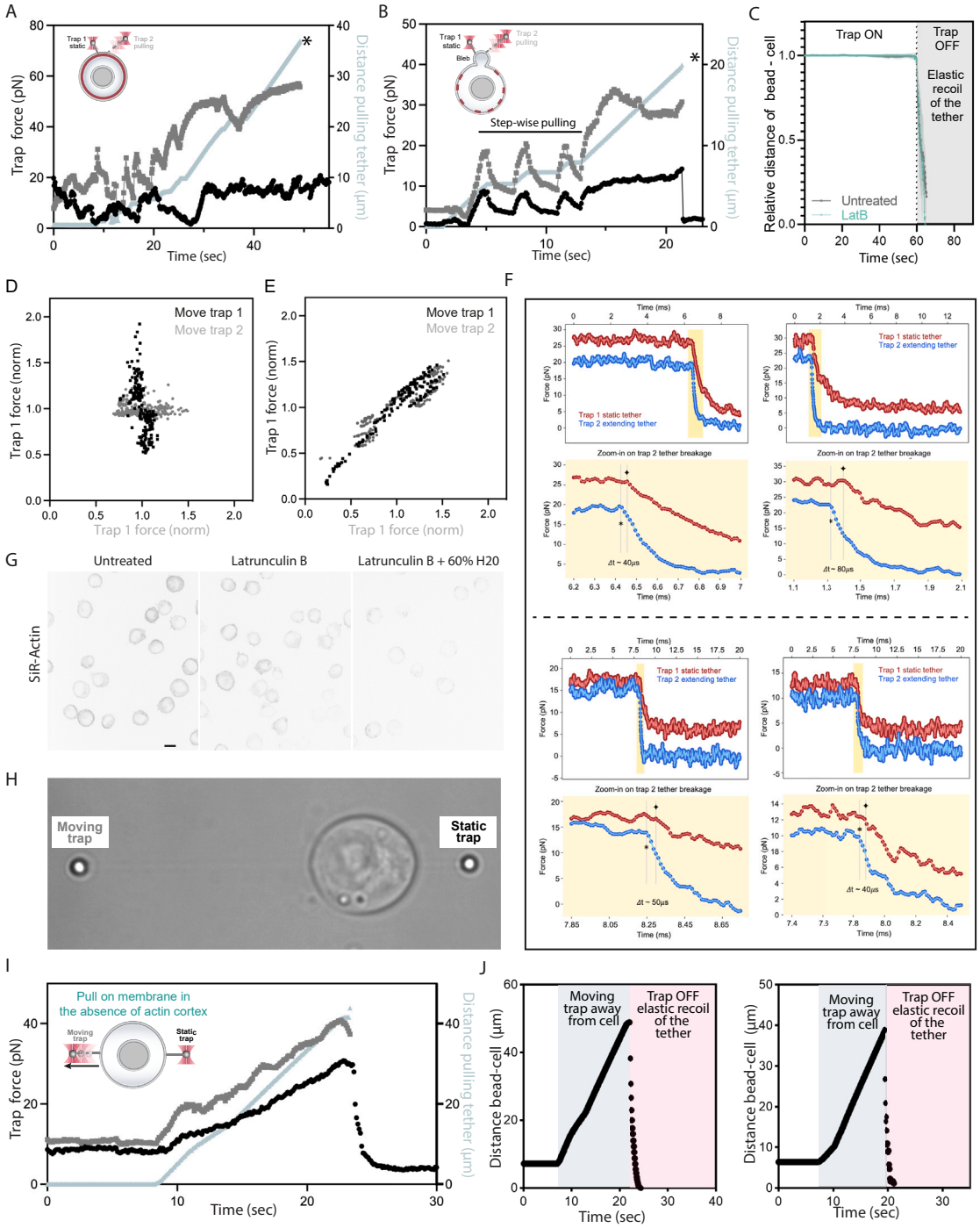

Figure S3. Mechanical perturbations affecting only the plasma membrane do not result in measurable membrane tension propagation in cells but do in blebs detached from actin cortex, related to Figure 3

(A) An example time trace of trap force for dual membrane tension measurements, where one moving trap (T2, blue) mechanically perturbs on the cell membrane by continuously pulling and extending the membrane tether, and the other trap remains static (T1, red) to monitor changes and propagation in tension to a nearby membrane tether. The increase in length of the extending tether from the cell body is plotted in gray along the right y axis. "*" annotates when the extending tether broke. Note that a sudden tension release upon breakage of the extending tether (blue, at t ~50 s) does not lead to changes in tension on the static tether (red), which is in close proximity to the extending tether ($\leq$2 μm). This observation shows that mechanical perturbations affecting only the plasma membrane in cells are locally constrained and inadequate to generate measurable tension propagation between the two tethers.

(B) Similar operations as (A) but monitoring tension propagation between two membrane tethers on cellular blebs (i.e., a vesicle-like, small section of membrane detached from actin cortex upon latrunculin B treatment). The tension readouts between the extending and the static tethers on blebs appear highly correlated,

(legend continued on next page)

unlike those on cell body in (A). Specifically, during the "step-wise pulling" to extend tether in trap 2 (blue), the static tether held in trap 1 (red) exhibits immediate spiky rises in tension, mirroring the pattern in trap 2. When a smooth increase is exerted on the extending tether by trap 2 (blue, at t ~ 13 s), the tension increase on static tether (red) accordingly becomes gradual. Furthermore, the sudden drop in tension back to initial level on the static tether (red, t ~ 26 s)—in response to the sudden tether breakage (*) and thus tension release of the extending tether (blue)—reflects a direct tension transmission and rapid propagation (see E) within a membrane bleb detached from the constraining actin cortex.

(C) Average time trace of relative distance between bead and cell in untreated cells and cells treated with 10 μM of the actin inhibitor latrunculin B. After tether pulling measurements, the trapping laser is turned off and the elastic recoil of the bead toward the cell is observed to confirm the absence of cytoskeleton in the tether. Similar tether recoil is observed between untreated and latrunculin-treated cells (means ± SD; n > 13, N > 3).

(D) Similar to (A) but we alternate which tether is pulling and which tether is static. Trap forces (readout of membrane tension response) from static tether is uncorrelated to that of moving tether (i.e., little to no change in tension on the static tether during pulling of the moving tether).

(E) Similar to (C) but probing tension in blebs (membrane detached from actin cortex); here, a high correlation is observed between static and moving tethers.

(F) Example zoom-in traces of dual trap forces (raw data at 78 kHz) showing the time difference between a sudden tension release upon breakage (*) of the extending tether (blue) and the subsequent reduction (✦) in tension on the static tether (red; traces slightly offset in y axis for illustration clarity). Typically, this time delay observed is ≤100 μs (measured between the inflection points, * and ✦, on each trace), which is right around the temporal resolution of our optical trapping instrument (limited by the corner frequency of a 2-μm bead held by a trap with stiffness of ~0.2 pN/nm), indicating that the actual timescale of tension propagation on cellular blebs is likely too fast to be resolved in our experiments.

(G) Representative confocal images of actin in cells using actin dye SiR-actin, comparing untreated cells as control with cells treated with either 10 μM of latrunculin B or with a combination of 10 μM of latrunculin B and in hypotonic media (+60% H20). Scale bar: 10 μM.

(H) Brightfield image of dual-tether pulling from opposite sides of a cell treated with a combination of 10 μM of latrunculin B and hypotonic shock.

(I) Representative force trace of a cell treated with a combination of 10 μM of latrunculin B and a hypotonic shock showing long-range membrane tension propagation in cells with heavily depolymerized cytoskeleton.

(J) Two example time traces of distance between bead and cell in cells treated with 10 μM of the actin inhibitor latrunculin B and with an hypotonic osmotic shock to heavily depolymerize the actin cytoskeleton. After tether pulling measurements, the trapping laser is turned off and the elastic recoil of the bead toward the cell is observed to confirm the absence of cytoskeleton in the tether. We observe similar tether recoil as with untreated and latrunculin-treated cells.

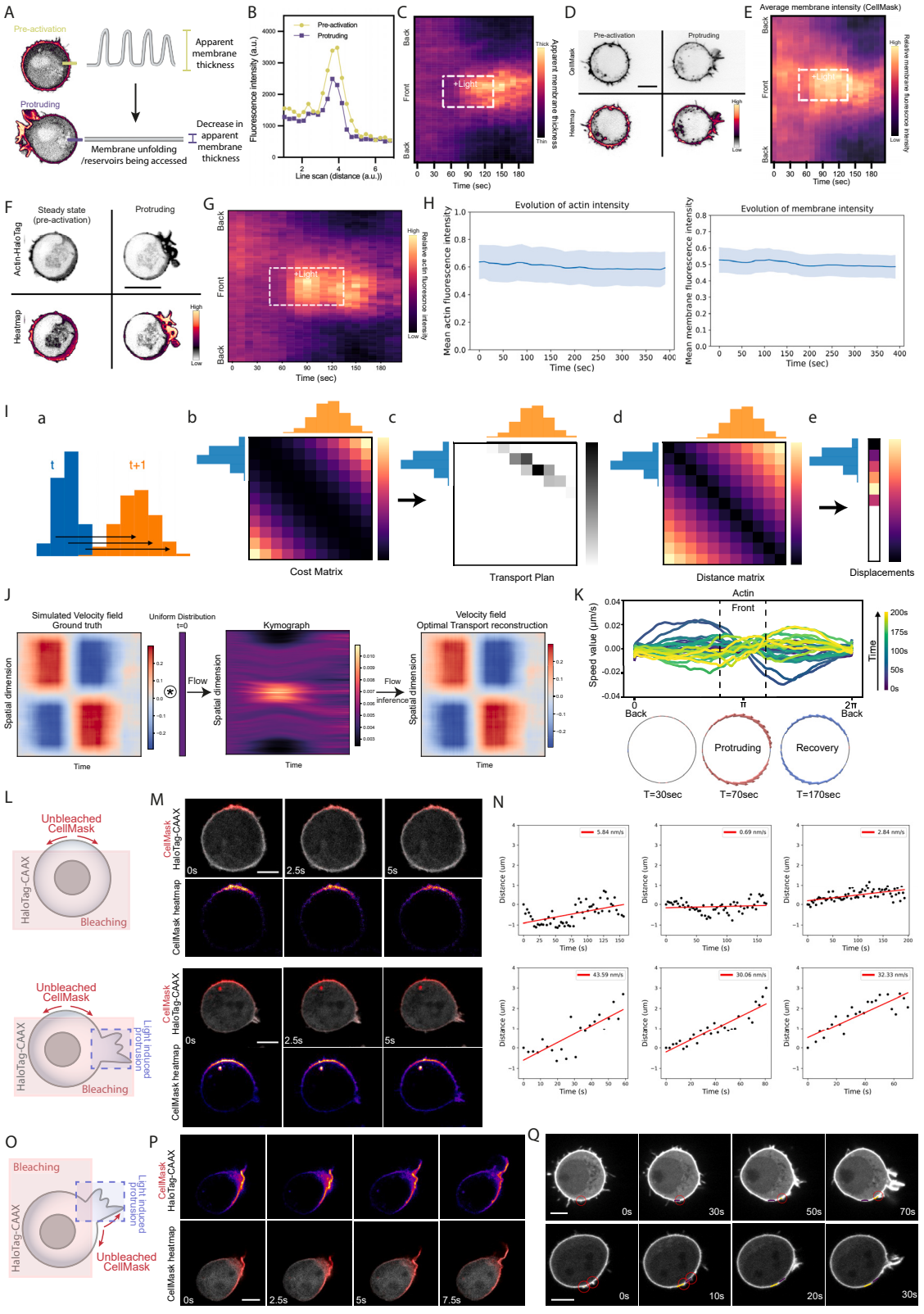

(legend on next page)

Figure S4. Long-range tension propagation coincides with directed membrane flows toward the protrusion, related to Figure 4

(A and B) Apparent membrane thickness is measured based on the width of fluorescence intensity profile across the cell contour, e.g., on the side of cell protrusion (black line). At steady state (pre-activation), the cell membrane contour appears rugged (top image) and thick in width (light green curve in B), likely due to the presence of membrane reservoirs. As the cell protrudes, the membrane intensity outside of the protruding region drops (bottom image) and becomes thinner in width (purple curve in B).

(C) Kymograph of averaged apparent membrane thickness along the normalized cell circumference (y axis) over time (x axis): before, during, and after localized light-activated protrusion (box in white dashed line). Apart from the protruding site, apparent membrane thickness reduces on average throughout the cell, likely reflecting a decrease in membrane reservoirs and a redistribution of extra membranes toward the protrusion site.

(D) Representative confocal images of an opto-PI3K cell stained with plasma membrane dye (CellMask) before light activation or during protrusion.

(E) Kymograph of membrane fluorescence intensity (from cells stained with CellMask) along the normalized cell circumference (y axis) over time (x axis): before, during, and after localized light-activated protrusion (box in white dashed line; $n > 25$, $N = 4$).

(F) Confocal images of opto-PI3K cells expressing actin marker (actin-HaloTag): before and during light-activated protrusion.

(G) Kymographs of actin fluorescence along the normalized cell circumference (y axis) show that over time (x axis) actin accumulates toward the protruding cell front and is depleted from the back ($n > 30$, $N = 6$; see STAR Methods).

(H) Left, evolution of the total membrane intensity across the cell contour (means ± SD; $n > 30$, $N = 6$). Except for a small intensity decrease due to the bleaching of the fluorophore, the membrane quantity is conserved. Right, evolution of the total actin intensity across the cell contour (means ± SD; $n > 50$, $N = 6$). Bleaching of the fluorophore across time is visible. Actin intensity is conserved across time, with a higher standard deviation than the membrane intensity.

(I) (a–e) An illustrative example of optimal transport between two discrete 1-dimensional distributions, at time t (blue) and time $t + 1$ (orange), which represent the amounts of membrane (or actin) along the membrane contour at two different time points. (a) Cost matrix C, in which C[i,j] indicates the value of the cost to displace an element from position i to the position j. Here, the cost function shown is the square of the curvilinear distance. (b) Transport Plan to go from the distribution at time t to the distribution at time $t + 1$, minimizing the total cost of the displacement, computed from the cost matrix in (a). (c) Distance matrix D, in which D[i,j] indicates the value of the distance between an element at the position i and an element at the position j. The distance chosen is the curvilinear distance. (d) The transport plan and the distance matrix allow to compute the mean displacement for every position between times t and $t + 1$. (e–g) Matrices in the case of periodic boundary conditions, such as the circular contour of the cell. (e) Cost matrix with periodic boundary conditions. The cost function chosen is still the square of the curvilinear distance, but as the topology of the curve is periodic, the matrix is changed to reflect this new topology. To keep track of the direction of the displacement, the distances can be positive or negative (and subsequently the positive and negative speed shown in Figures 4D and 4E). A displacement in the clockwise direction (increasing angle coordinate) is positive, whereas a displacement in the counter-clockwise direction is negative.

(J) Pipeline and example of flow inference validation using computer simulated distributions (see Methods S1). Using Optimal Transports, flows are inferred with minimal errors.

(K) (Top) Actin flow field inferred from kymograph intensity change over time using optimal transport. (Bottom) Actin flow around the cell as inferred by optimal transport before, during, and after (t = 30, 70, and 170 s) right-side protrusion; the flow magnitude is denoted by the arrow size (red: forward flow, blue: backward).

(L) Alternative membrane diffusion assay in which we sequentially bleach the membrane marker CellMask across a wide section of the cell, opto-activate the cell on the side of the unbleached area and monitor the diffusion pattern of the unbleached area over time. We use cells with no activating light as control.

(M) Example confocal images of the membrane markers HaloTag-CAAX and CellMask in a cell with no activating light (control, top) and a light-induced protruding cell (bottom).

(N) Quantification of shift centroid of signal intensity in control cells (top, no apparent flow) and protruding cells (bottom, biased flow toward side of protrusion).

(O and P) Similar to (L and M) but with an overlap between the unbleached and activation area.

(Q) Two examples of microvilli tracking during light-induced cell protrusion. Tracked microvilli are circled in red and their trajectory is represented by lines of different colors. Scale bars: 5 μm.

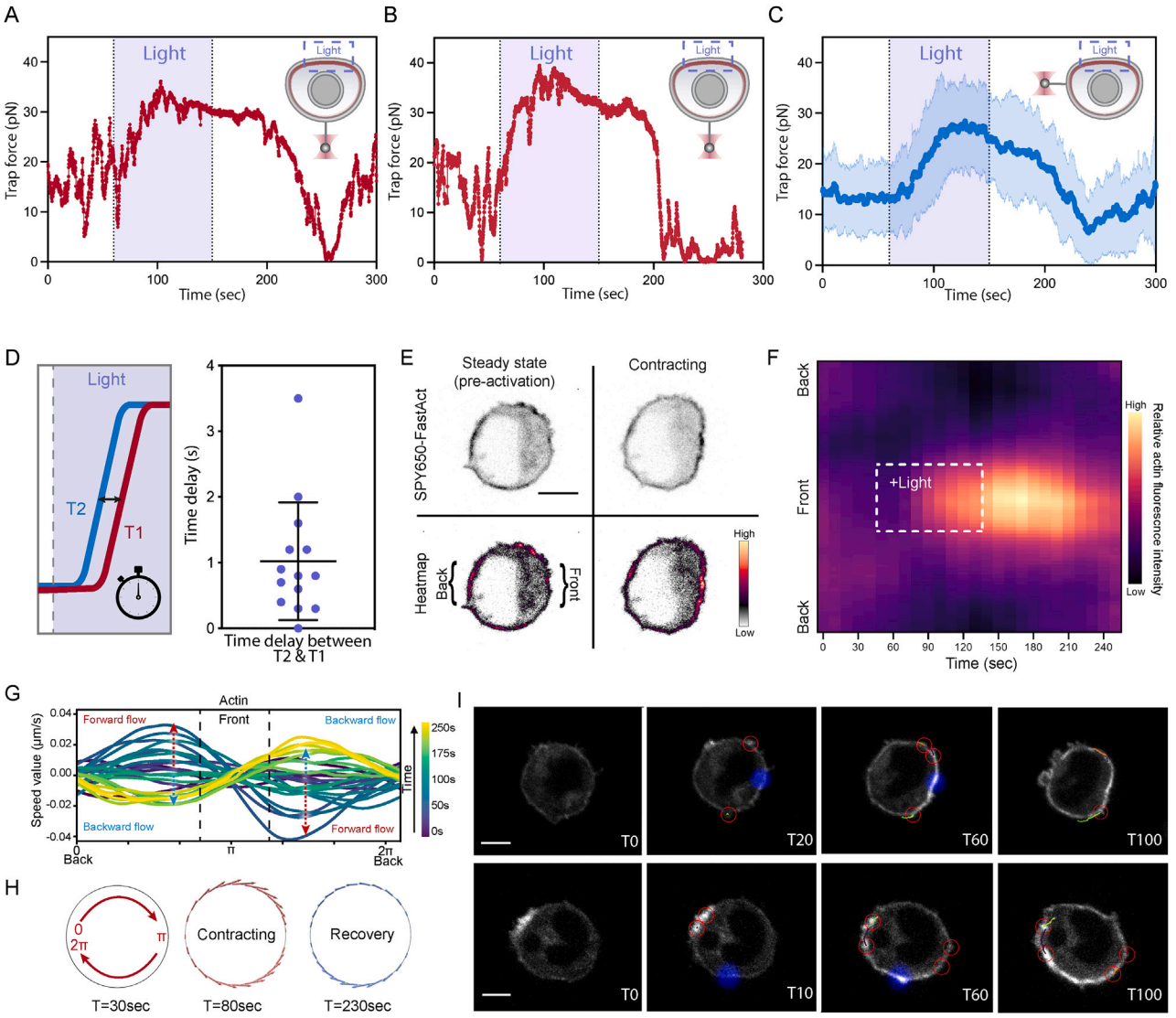

Figure S5. Optogenetically induced actomyosin contractions generate rapid long-range membrane tension propagation and actin flows, related to Figure 5

(A and B) Representative time traces of trap force (a direct readout of cell membrane tension change) during light-induced actomyosin contraction. Revealing robust increase in membrane tension during light-activated contractions on the opposite end of the cell; light: 90 s on (shaded area).

(C) Averaged time trace of trap force before (steady state), during (Light), and after activating cell contraction, measured at the side (90°) of the contraction (means ± SD; n > 30, N = 7).

(D) (Left) Time delay measured between tension rise on membrane tethers adjacent to (trap 2 at 90°, blue) and opposite from (trap 1 at 180°, red) cell contraction. (Right) In most cells, the traps detect membrane tension increase on both tethers within a second or less of one another, indicating a rapid propagation of tension across the cell. Error bar: means ± SD.

(E) Confocal images of opto-LARG cells stained with actin marker (SPY650-FastAct): before and during light-activated contraction.

(F) Average kymograph of relative actin fluorescence intensity along the normalized cell circumference (y axis) show that over time (x axis). Actin accumulates toward the contracting cell front (n > 25, N = 3; see STAR Methods).

(G) Actin flow field inferred using optimal transport from kymograph intensity changes over time: shortly after activation begins (t = 120 s, teal traces), the magnitude of membrane flow speed increases (red dashed arrows), with positive speed for clockwise flow along the cell upper half and negative speed for counter-clockwise flow along the bottom half, all moving toward the cell contracting front (π). During recovery (t = 230 s, light yellow traces), the direction of membrane flow reverses (blue dashed arrows).

(H) Actin flow around the cell before, during, and after (t = 30, 80, and 230 s) right-side contraction; the flow magnitude is denoted by the arrow size (red: forward flow, blue: backward). Membrane flows toward the contraction in the contracting phase and away from the protrusion during the recovery phase.

(I) Two examples of actin speckle tracking during light-induced cell contraction. Tracked actin patches are circled in red and their trajectory is represented by lines of different colors. Scale bars: 5 μm.

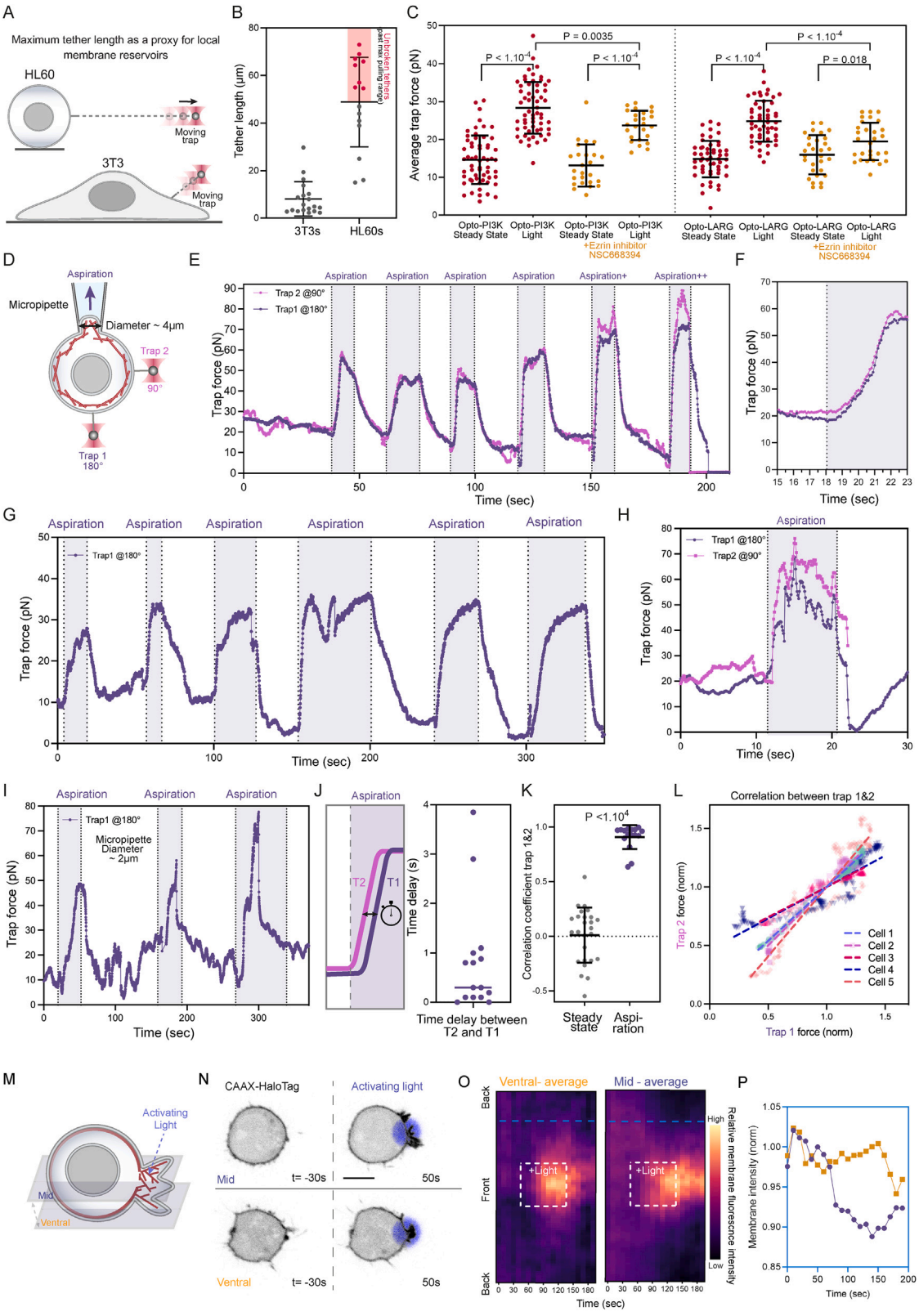

(legend on next page)

Figure S6. Mechanical perturbations applied on both membrane and cortex lead to rapid tension propagation across the cell, related to Figure 6

(A) Tether pulling assay in which tethers are pulled at constant speed until they break. Maximum tether length is used as a proxy for local membrane reservoirs[56].
(B) Maximum tether length comparison of 3T3s fibroblasts versus HL-60s cells. In red are cells for which the maximum pulling length was reached on our setup without tether breaking occurring, suggested high local membrane reservoir availability. Error bar: means ± SD; n > 15, N > 3.
(C) Average trap force of different opto-cells (OptoPI3K-based protrusion induction and OptoLARG-based actomyosin contractility), before and after light in the absence or presence of the Ezrin inhibitor NSC668394 (25 μM). These data show that lowering MCA only slightly affects membrane tension increase in protruding cells but severely impedes membrane tension increases in contracting cells. Error bar: means ± SD; p values from Welch's unpaired Student's t test (n > 25, N > 3).
(D) A dual-tether pulling assay to simultaneously monitor membrane tension on the far end (bottom, trap 1 at 180°) and on the side of the cell (right, trap 2 at 90°) during micropipette aspiration (top, ~4–5 μm in tip diameter), which mechanically pulls on both the membrane and actin cortex underneath.
(E) Representative time traces of dual trap forces over successive cycles of aspiration (shaded area) and relaxation; the magnitude of aspiration progressively increased in the last two cycles (+ and ++; the first three cycles were also shown in Figure 6I). The nearly superimposable tension rise and fall on the two membrane tethers show that membrane tension propagates rapidly across the cell upon mechanical perturbations exerted to both the cortex and membrane. Note that the profiles of tension rise upon aspiration and of tension drop during relaxation resemble those observed with light-activated actin-driven protrusions (Figure 2B).
(F) Zoom-in on the first aspiration event shows that the trap force for membrane tension on the tether closer (pink) to the aspiration site started increasing slightly earlier and ended up slightly higher compared with that measured on the tether opposite from the aspiration (purple).
(G) An example trace of tether tension response monitored on the opposite side of micropipette aspiration (trap 1 at 180°). Here, the recording lasted for six rounds of aspiration and relaxation.
(H) Another example of dual-tether membrane tension measurement upon micropipette aspiration; the tether in trap 2 broke (*) shortly after the aspiration stopped.
(I) An example time trace of trap force for cell membrane tension exhibits robust responses over three aspiration cycles using a micropipette of slightly smaller diameter (~2 μm).
(J) (Left) Time delay measured between tension rise on membrane tethers adjacent to (trap 2 at 90°, pink) and opposite from (trap 1 at 180°, purple) cell aspiration using micropipettes. (Right) In most cells, the traps detect membrane tension increase on both tethers within a second or less of one another, indicating a rapid propagation of tension across the cell.
(K) Pearson correlation coefficient between dual trap forces measured before any perturbations (steady state) and during mechanical pulling upon micropipette aspiration. Error bar: means ± SD; p values from Welch's unpaired Student's t test (n > 15, N > 3).
(L) Correlation plots of normalized trap forces between the two tethers during micropipette aspiration. Five representative measurements from different cells are shown; dashed lines: linear regression.
(M) Comparing membrane flows of light-induced protrusions at the mid and ventral plane of the cell.
(N) Confocal images of a cell membrane (visualized using CAAX-HaloTag) before and during protrusion at two different z planes (mid-section and ventral plane of the cell). Scale bar: 5 μm.
(O) Average kymograph of relative membrane fluorescence intensity along the normalized cell circumference (y axis) at the ventral and mid-plane of the cell over time (x axis) showing a decreased membrane flow at the ventral side of the cell, likely due to friction between the cell and the substrate (n > 30, N = 3).
(P) Normalized membrane fluorescence intensity across the blue dotted line in (O).